Development of a generalisable tryptophan-optimised quenchbody biosensor based on a synthetic nanobody library

Author list:

Jordan H. Cater[1], Nehad S. El Salamouni[1*], Ghada H. Mansour[2*], Sebastian Hutchinson[2*], Conall Mc Guinness[1*], Stefan H. Mueller[1], Richard R. Spinks[1], Nirukshan Shanmugam[1], Adeline Pichard-Kostuch[2], Viktor Zahoransky[2], Harshad Ghodke[1], Marco Ribezzi-Crivellari[2], Haibo Yu[1,3], Antoine M. van Oijen[1†], Andrew D. Griffiths[2†] and Lisanne M. Spenkelink[1†]

[1]Molecular Horizons, School of Chemistry and Molecular Bioscience, University of Wollongong, Wollongong, NSW 2522, Australia
[2]Laboratoire de Biochimie, Chimie Biologie et Innovation, ESPCI Paris, Université PSL, Paris, France
[3]ARC Centre of Excellence in Quantum Biotechnology, University of Wollongong, Wollongong, NSW 2522, Australia

*Denotes equal contribution

†Correspondence to vanoijen@uow.edu.au, andrew.griffiths@espci.fr and lisanne@uow.edu.au

Abstract

Quenchbodies are antibodies labelled with a fluorophore that increases in intensity upon antigen binding, which makes them promising candidates for the development of diagnostic or other immunoassays requiring antigen quantification. Quenchbodies based on camelid nanobodies are particularly attractive for rapid development of immunoassays against molecular antigens of interest, due to their small size, ease of expression, high stability, rapid evolvability, and amenability to protein engineering. However, current nanobody-based quenchbodies typically display only modest fluorescence increases when binding to protein antigens (≤ 1.1–1.7-fold), with few examples reaching > 2-fold. In contrast to single-chain variable region (scFv; 32 kDa) or antigen-binding fragment (Fab; 50 kDa) quenchbodies, where semi-conserved tryptophans at the VH-VL interface quench the fluorophore, here we show that tryptophan residues in the nanobody complementarity-determining regions (CDRs) are critical to fluorescence antigen detection. This informed the development of a synthetic convex-binding nanobody library containing conserved tryptophans in the CDRs, which was used for the *in vitro* selection and affinity maturation of novel quenchbodies against human inflammatory cytokine interleukin 6 (IL6). Initial *in silico* modelling and biochemical analyses showed that existing nanobodies for maltose-binding protein (MBP) and lysozyme could be converted into quenchbodies (Qb-MBP and Qb-Lys), with fluorescence fold-increases of 1.5 and 1.3, respectively, when recognising their cognate antigen. Rational mutational substitution of tryptophans into the CDR-region of the quenchbodies resulted in fluorescence fold-increases of 1.9 and 1.6 for Qb-MBP (Y59W/Y114W) and Qb-Lys (Y110W), respectively, supporting the importance of CDR-based tryptophans in the nanobody quenchbody mechanism. A synthetic nanobody library containing conserved CDR-based tryptophans was then created, selected, and affinity matured using a completely *in vitro* SNAP-display system, yielding quenchbodies against interleukin-6 (IL6) with enhanced fluorescence fold-increases of 1.5–2.4 (EC_{50} = 20–1,113 nM binding affinity). The ease and speed by which nanobody-based quenchbodies can be discovered using this completely *in vitro* selection strategy based on a single synthetic library, makes this a very attractive approach to develop immunoassays for detection of a wide range of molecular targets, including proteins.

Introduction

The detection of disease biomarkers is important in all aspects of modern medicine. Detection of proteinaceous molecules is particularly important as it often connects with disease phenotypes directly due to the functional output of proteins occurring on second to minute timescales. This is unlike genetic signatures which may be uncoupled from disease phenotypes due to epigenetics or other forms of regulation, with a multi-omics approach becoming the preferred method for accurate disease monitoring into the future, especially for complex diseases like cancer [1]. Analytical mass spectrometry is the gold standard for study of the proteome and identification of proteinaceous biomarkers, and is extensively reviewed elsewhere [2-4]. However, mass spectrometry typically requires large and expensive equipment, and involves lengthy and complex analysis for detection. Immunoassays, which rely on the affinity and specificity of antibodies for antigens are, on the other hand, advantageous to detect specific biomarkers due to their ease of use, rapid results, target selectivity, sensitivity, and affordability. Advancements in synthetic antibody selection and evolution have also opened avenues for the rapid development of immunoassays that recognise a broad range of targets, without the lengthy lead times or batch-based inconsistencies inherent to the generation of animal-origin and/or cell-based monoclonal antibodies [5-8]. These features make immunoassays of high interest for developing rapid capabilities in monitoring disease-related protein biomarkers in research and clinical settings, especially for being able to quickly adapt to the challenges of future health issues like pandemics.

Analyte detection in immunoassays can be based on a variety of output signals, including enzyme reaction monitoring, fluorescence, chemiluminescence, and chromatographic separation [9, 10]. Regardless, immunoassays can be generally dichotomised into heterogenous or homogenous depending on whether the antibody-bound label responsible for antigen detection requires separation from the free unbound antibody-bound label (heterogenous), or not (homogenous). The enzyme-linked immunosorbent assay (ELISA) is a well-known example of a heterogenous immunoassay relying on enzyme output that is often used in research and clinical settings [11]. Lateral flow assays are another type of common heterogenous immunoassay which has become increasingly popular in recent years, especially in point of care settings due to their speed and ease of use [12]. However, heterogenous immunoassays typically require lengthy incubation times and extensive washes, making analyte detection laborious and time consuming. Comparatively, homogenous “mix-and-read” immunoassays are quicker and simpler, provided the sample matrix does not interfere with the immunoassay. AlphaLISA (Perkin Elmer) is an example of a homogenous ELISA-style immunoassay that seeks to overcome laborious procedures associated with traditional ELISAs [13]. However, sandwich ELISA, lateral flow assays and AlphaLISA typically require a characterised pair of antibodies that can simultaneously bind the antigen at two different epitopes, which is considered the major bottleneck in development of all sandwich-style immunoassays [12, 14]. Conversely, another homogenous immunoassay requires only a single fluorescently-labelled antibody molecule for analyte detection, called a “quenchbody”.

Quenchbodies and their working principles are reviewed in detail elsewhere [15-17]. Briefly, quenchbodies are typically single-chain variable regions (scFv; 32 kDa) or antigen-binding fragments (Fab; 50 kDa) of antibodies, which have been labelled with a fluorophore, via a flexible peptide linker usually at the N-terminus of the antibody. This flexible linker permits the fluorophore to interact with tryptophan residues in the quenchbody. This interaction leads to a reduction in fluorescence intensity (quenching), through photoinduced electron transfer (PET), facilitated by hydrophobic/π-π stacking interactions, provided the fluorophore is within ≤ 10 Å of the quenching tryptophan [18-20]. The quenched fluorophore can increase in fluorescence intensity when it is prevented from interacting with the tryptophan. This can occur by (i) binding of the quenchbody to the cognate antigen, which sterically hinders the fluorophore from binding to tryptophan in hydrophobic pockets, or (ii) denaturing the quenchbody with chaotropic agents. The increase in fluorescence intensity of the quenchbody on antigen binding can be used as a homogenous immunoassay to rapidly measure concentration of antigens, even in complex biological samples such as human plasma [21, 22].

Most current quenchbodies are based on scFv and Fab, but quenchbodies based on single-domain nanobodies derived from camelids are rare, despite nanobodies possessing several key advantages. These include small size (~ 15 kDa), ease of expression, high stability, evolvability, and amenability to protein engineering [23]. Nanobody-based quenchbodies are particularly effective for recognition of smaller antigens like small-molecule drugs or peptides [24], with a maximal 6-fold increase in tetramethylrhodamine (TAMRA) fluorescence intensity observed in one case upon binding of a quenchbody to methotrexate [21]. However, recognition of larger protein antigens generally has poorer responses due to the protein antigen being able to quench the fluorophore of the quenchbody [24], with fluorescent fold-increases of 1.1-1.7 observed for albumin [15, 22], claudin [25], human epidermal growth factor receptor-2 (HER2) [26], and hemagglutinin [27]. Although variable fluorophore quenching by different protein antigens is an inherent problem which could contribute to poorer quenchbody performance, optimisation of the position of key-nanobody tryptophans relative to the fluorophore is likely to yield improvements to the performance of nanobody-based quenchbodies.

We therefore sought to create a generalisable nanobody-based quenchbody scaffold containing tryptophans in optimal positions, which would be capable of recognising protein antigens with superior performance. TAMRA was chosen as the fluorophore given its superior performance over similar dyes in nanobody-based quenchbodies [21], while lysozyme-binding and maltose-binding protein (MBP)-binding nanobodies (Qb-Lys and Qb-MBP, respectively) were chosen for conversion into quenchbodies, given the availability of high-resolution structures to facilitate structural-mechanistic modelling *in silico* (PDB IDs: 5M14 and 1ZVH) [28, 29]. After initial modelling revealed the importance of intrinsic tryptophan locations, Qb-MBP and Qb-Lys were subjected to rational mutagenesis involving substitution of antigen-contacting tyrosines with tryptophans in an attempt to improve fluorophore-quenching. High-performing tryptophan mutations informed the design of a library of nanobodies containing conserved tryptophans in CDRs which was selected *in vitro* against interleukin-6 (IL6), resulting in the production of a nanobody-based quenchbody which had a

maximal 2.4 fold-increase in TAMRA fluorescence intensity when detecting IL6 antigen, representing a current improvement in this class of quenchbodies. We envisage this high-performance nanobody-based quenchbody will form a generalisable scaffold suitable for selection of quenchbodies for detection of a variety of chosen clinical protein antigens via rapid immunoassays.

Methods

In silico modelling and molecular dynamics simulations of quenchbodies

Initial co-ordinates to inform quenchbody design were obtained from PDB ID: 1ZVH [28] and 5M14 [29], corresponding to the X-ray structures of lysozyme-binding nanobody (Qb-Lys) and MBP-binding nanobody (Qb-MBP). N-terminal Cys-tags were modelled using Modeller (version 10.2) [30]. Systems were set up using CHARMM-GUI [31]. The CHARMM36m protein force field was used for proteins. The CHARMM General Force Field (CGenFF) generated using the CGenFF interface at parachem.org (https://cgenff.umaryland.edu) [32] was used for the fluorophore, TAMRA. The TIP3P model was used for water [33]. Simulations were carried out using NAMD 3.0 (Nanoscale Molecular Dynamics, version 3 alpha) [34].

Simulations were performed after solvating the system in an octahedral box that extended at least 12 Å from the solute interface. Na^+ and Cl^- counter ions were added to neutralise the system and achieve a salt concentration of 0.15 M. pKa calculations were performed using PROPKA [35] to assign protonation states of ionisable residues. Simulations were performed using periodic boundary conditions (PBC) at constant temperature (303.15 K) with the Langevin algorithm (a damping coefficient of 1/ps) [36] and at a pressure of 1.0 bar using the Nose-Hoover Langevin Piston method [37]. Hydrogen mass repartitioning [38] was applied with the time step set to 4.0 fs and all covalent bonds involving hydrogens were kept rigid with the RATTLE algorithm [39]. Short-range electrostatics were calculated together with long-range electrostatics particle mesh Ewald (PME) [40] with a cut-off of 9.0 Å and a PME grid size of 1.0 Å. For all systems, energy minimisation (10,000 steps) and 125 ps equilibration were performed first with positional restraints placed on all the protein-heavy atoms (with a force constant of 1.0 kcal/mol/$Å^2$ on the backbone atoms and 0.5 kcal/mol/$Å^2$ on the side chain atoms) and TAMRA heavy atoms (with a force constant of 0.5 kcal/mol/$Å^2$). This was followed by 12 and 6 µs production runs for the apo and antigen-bound quenchbodies, respectively. Six independent replicates for each system were simulated, with a total of 72 µs for the apo state and 36 µs for the antigen-bound states. Initial structures for the simulations were the top 3 modelled Cys-tag structures based on DOPE scores with attached TAMRA(R) or TAMRA(S). Snapshots were saved every 100 ps. VMD (Visual Molecular Dynamics) [41], LOOS (Lightweight Object-Orientated Structure Analysis) [42], MDAnalysis [43] and UCSF Chimera [44-46] were used to analyze and visualise the trajectories. Quenching distances were measured between the centres of masses of each of the tryptophans and TAMRA. FoldX was used to predict the effects of residue mutations on quenchbody stability and antigen binding [47].

DNA and protein sequence design of quenchbodies

Protein coding sequences from either the MBP-binding nanobody or the lysozyme-binding nanobody were designed with (i) an N-terminal Cys-tag as a target for fluorophore labelling, (ii) a C-terminal Avi-tag to enable biotinylation, and (iii) a 3 x FLAG-tag and 10 x His-tag to facilitate purification procedures. The entire protein coding element was then converted to DNA and codon optimised using IDT's *Escherichia coli* (*E. coli*) B strain optimiser. This protein-coding DNA element was then combined into a gene expression cassette featuring a flanking T7 promoter and terminator for cell-free *in vitro* transcription and translation (IVTT) of the protein product and ordered as a Geneblock from IDT. The Geneblock also featured flanking DNA elements suitable for polymerase chain reaction (PCR) replication of the Geneblock, specifically DNA complementary to the forward primer 5'- ACCCGGCATGACAGGAG-3' and the reverse primer 5'-GTGGCGGCCGCTCTA-3'. PCR replication of Geneblocks was conducted using Q5® Hot Start High-Fidelity Master Mix (NEB; as per the manufacturer's instructions) at a scale of 100 µL, using 50 ng of Geneblock as template and 0.5 µM of forward and reverse primer in a PCR Mastercycler (Eppendorf), with initial heating at 98°C for 30s, followed by 32 cycles of denaturation (98°C, 10 s), annealing (60°C, 30 s), and extension (72°C, 15 s). Quenchbody PCR products were purified using Wizard Clean up kits (Promega; as per the manufacturer's instructions) and were quantified by A_{260}/A_{280} absorbance on a Nanodrop 2000C spectrophotometer (ThermoFisher. Quenchbody PCR products were further analysed by agarose gel electrophoresis to ensure PCR products were of the expected size and purity before they were used for IVTT. All mutant quenchbodies were generated by *in silico* sequence modification of 5M14 and 1ZVH quenchbody constructs and re-ordered as Geneblocks from IDT.

In vitro quenchbody expression, labelling and purification

For each quenchbody, 600 ng of purified PCR product was combined with NEBExpress® Cell-free *E. coli* Protein Synthesis System (NEB) [48] at 2 x the reaction scale, including protein disulfide bond enhancer (NEB) and GamS (NEB), as per the manufacturer's instructions, and incubated for 16 h at room temperature with shaking at 1200 rpm in a Thermomixer (Eppendorf; used for all subsequent shaking and incubation steps). Expressed quenchbodies were then purified from the crude IVTT mixture (100 µL) by combining with 12.5 µL of Pierce Anti-DYKD4K (FLAG) Magnetic Agarose beads (equivalent to 50 µL of original resuspension) prewashed in phosphate-buffered saline (PBS) using a MagJET separation magnet (used for all subsequent wash steps). The crude IVTT-FLAG bead mixture was then mixed at room temperature for 30 min, 1200 rpm, to allow binding of the FLAG-tagged quenchbody to the beads, and subsequently washed with 0.2 mL PBS. In MBP-binding quenchbodies, the beads were subjected to an additional wash with 0.2 mL of 0.5 M maltose dissolved in PBS to remove endogenous MBP (present in the endogenous *E. coli* cell-free lysate as a contaminant), as maltose competes with the nanobody for MBP-binding [29]. The beads were then washed with 100 uL of 1 mM tris(2-carboxyethyl)phosphine (TCEP) in PBS for 10 min at 16°C with shaking at 1200 rpm, followed by washing with 0.2 mL of degassed PBS. Beads were immediately combined with 100 µL of 250 µM 5(6)-carboxytetramethylrhodamine (TAMRA) maleimide with C6-linker dissolved in degassed PBS at a final concentration of 1% (v/v)

dimethylsulfoxide (DMSO), and incubated for 3 h (room temperature, 1200 rpm). Beads were then subjected to 9 x 0.2 mL washes with PBS to remove unconjugated dye. Finally, quenchbodies were eluted from the beads using 50 µL of 1.5 mg/mL Pierce™ 3 x DYKDDDDK Peptide (ThermoFisher).

SDS-PAGE and in-gel fluorescence analysis

Proteins were diluted in 2 x denaturing Tris-glycine sample buffer to a final concentration of 63 mM Tris-HCl, 10% (v/v) glycerol, 5% (v/v) β-mercaptoethanol (BME), 2% (w/v) sodium dodecysulfate (SDS), 0.0025% (w/v) bromophenol blue, pH 6.8, and subjected to SDS-polyacrylamide gel electrophoresis (SDS-PAGE) at 150 V for 30 min using Mini-PROTEAN TGX precast gels in a Tetra electrophoresis system filled with Tris-glycine running buffer (25 mM Tris, 192 mM glycine, 0.1% (v/v) SDS, pH 8.3), according to the manufacturer's instructions (BIO-RAD, Gladesville, Australia). Protein size was estimated using Precision Plus Dual Colour Protein Standards (BIO-RAD). All gels were stained overnight with Instant Blue (Expedeon, Cambridge, UK) and subsequently destained in MilliQ H_2O overnight before being imaged on a Gel Doc XR+ Molecular Imager (BIO-RAD). In-gel TAMRA fluorescence of quenchbodies following SDS-PAGE was analysed on an Amersham Typhoon Biomolecular Imager (Cytiva), using the preset acquisition settings for Cy3 imaging (excitation = 532 nm, emission filter = 570 ± 20 nm).

Pulldown binding assays

To assess their antigen binding, quenchbodies were expressed as above and were purified from the crude IVTT mixture (100 µL) by combining with 12.5 µL beads/50 uL suspension of Pierce Anti-DYKD4K (FLAG) Magnetic Agarose (30 min, 1200 rpm). The crude IVTT-FLAG bead mixture was then mixed at room temperature for 30 min, 1200 rpm, to allow binding of the FLAG-tagged quenchbody to the beads, and subsequently combined with 100 µL of (i) 1 µM MBP for MBP-binding quenchbodies, or (ii) 10 µM lysozyme for lysozyme-binding quenchbodies, and incubated for 30 min (room temperature, 1200 rpm). Beads were then subjected to 6 x 0.2 mL washes with PBS to remove any unconjugated or non-specifically bound antigen, and finally eluted with 50 µL of 1.5 mg/mL Pierce™ 3 x DYKDDDDK Peptide. The eluted quenchbody-antigen complex obtained by FLAG-pulldown was subjected to reducing SDS-PAGE and the effect of mutations on antigen binding was semi-quantitatively analysed by comparison to the binding of the wild-type (WT) control.

Protein:TAMRA Quantification

Protein concentration of TAMRA-labelled quenchbodies was quantified by A_{280} absorbance on a Nanodrop 2000C spectrophotometer, and was corrected against a FLAG peptide standard in PBS subjected to the same elution procedures to correct for background absorbance associated with the FLAG peptide. Protein concentration was further calculated by including the correction factor for TAMRA (A_{280} = 0.178) and assuming an extinction coefficient based on the polypeptide sequence properties calculated in ExPaSy ProtParam

[49]; (approximately ε = 47,000 cm^{-1} M^{-1} for quenchbodies). TAMRA concentration of TAMRA-labelled quenchbodies was determined by further A_{555} quantification assuming an extinction coefficient of 90,000 cm^{-1} M^{-1} for TAMRA.

Fluorescence spectrophotometry plate assays

Quenchbodies were diluted to 20 nM in PBS/0.05% (v/v) Tween-20 (PBST) in the absence or presence of 8000, 4000, 2000, 1000, 500, 250, 125, 64, 32, 16, 8, 4, 2, or 1 nM cognate antigens (lysozyme, MBP, or IL6), or 2% (w/v) SDS with 5% (v/v) β-mercaptoethanol (BME) as denaturant, and incubated for 1 h at room temperature. Samples were subsequently dispensed (n = 3, 40 µL/well) into black 384-well Griener microplates and analysed by fluorescence spectrophotometry in a CLARIOstar microplate reader with excitation = 535 ± 20 nm and emission = 585 ± 30 nm, using a dichroic filter of 557.5 nm. To compare fluorescence increases that occur in the presence of various concentrations of antigen ("fold-sense") or denaturant ("fold-quench"), all raw fluorescence values were normalised as a ratio to the 0 nM quenchbody control lacking any antigen or denaturant. To derive a quenchbody binding affinity, the fluorescence signal of quenchbody with 0 nM antigen was subtracted from all other samples containing antigen and the data was fitted to an equation describing a single site-specific binding mode with Hill slope to derive an equilibrium dissociation constant (K_D) in GraphPad Prism 9.4.0. The WT Qb-MBP was expressed and tested on three separate occasions including temporal separation between replicates, and showed essentially identical results across replicates, indicating biological replicates were redundant when studying any of the other mutants in the study.

Preparation of microfluidic flow cells

Flow chambers for microscopy were prepared as previously described [50-52]. Briefly, cover slips (24 × 24 mm, Marienfeld) were functionalised with biotin-PEG (Laysan Bio). A polydimethylsiloxane (PDMS) block was made using soft lithography methods and placed on top of the cover slips, creating a 1-mm wide and 0.1-mm high channel with a volume of 1 µL. Two stretches of polyethylene tubing (PE-60: 0.76-mm inlet diameter and 1.22-mm outer diameter, Walker Scientific) were inserted into the PDMS block at the entrance and exit of the channel to allow for buffer flow. Before the start of experiments, the flow channel was incubated with blocking buffer for 30 min (20 mM Tris–HCl pH 7.5, 50 mM NaCl, 0.0025% (v/v) Tween-20, 0.5 mg/mL bovine serum albumin, 2 mM ethylenediaminetetraacetic acid) to minimise nonspecific binding of proteins to the cover-slip surface. A syringe pump (Adelab Scientific) was used to introduce solutions to the flow cell. Prior to experimental acquisition, fields of view to be imaged were defined in the acquisition software (NIS-expand) and exposed to a high laser power to pre-bleach the surface before loading with fluorescent quenchbody. Qb-MBP was immobilised via biotin-streptavidin interaction on the coverslip by flowing a 10 pM solution in running buffer (10 mM phosphate buffer, 137 mM NaCl, 2.7 mM KCl, 40 ug/mL bovine serum albumin, 0.001 % (v/v) Tween-20, 10 mM ascorbic acid, pH 7.4) at 20 µL/min for 5 min, or until a density of approximately 1000 particles was obtained in one field of view (86 μm^2). Unbound quenchbody was subsequently removed by flowing running

buffer at 100 µL/min for 1 min. The 'before' condition was acquired in running buffer under a flow of 20 µL/min for 10 frames. For the 'after' condition, running buffer was applied at 100 µL/min for 1 min to ensure fast buffer exchange, then conditions consisting of either running buffer containing antigen, or 1% (v/v) SDS denaturant in MilliQ H_2O, were applied at 20 µL/min for 15 min. 'After' images were then acquired identical to 'before' conditions under 20 µL/min flow. Each condition tested is representative of at least 3 technical replicates preformed on different days using the same Qb-MBP stock.

TIRF microscopy

The flow cell device was mounted on an inverted total internal reflection fluorescence (TIRF) microscope (Nikon Eclipse Ti-E), with a 100 x TIRF objective (NA = 1.49, oil, Nikon). Samples were illuminated using a 532-nm laser (Coherent, Sapphire 532 CW) at 8.3 W/cm^{-2}. Fluorescence was captured with an EMCCD camera (Andor iXonLife 897) through a band pass emission filter (ET600/50 M, Chroma). For all measurements samples were visualised with an exposure time of 100 ms and an approximately equivalent frame-rate (excluding read time), unless otherwise specified.

Single-molecule Qb-MBP analysis

'Before' and 'after' movies (10 frames each) for each field of view were concatenated to make a single 20 frame file (n = 10 fields of view). Analysis was done using James' Immobilised Microscopy Suite (freely available at https://github.com/lilbutsa/JIM-Immobilized-Microscopy-Suite). Movies were drift corrected and particles were detected using a subaverage of the entire movies. This means that any particles present in either the 'before' or 'after' condition will be detected, which proved the most unbiased way to detect particles, whilst also accounting for appearance or disappearance of particles throughout the experiment. This analysis gave a csv output of intensity values over 20 frames for each detected particle, known as a trajectory. Mean intensity values from 'before' and 'after' were calculated, and the mean ratio increase of the 'after' to 'before' conditions was taken as a fold-sense value for an individual particle. In practice, this is the brightness increase of the particles between conditions. Fold-sense of the particles from each treatment were pooled and plotted on a probability density function to visualise the distribution of fold sense values in the population. Fold sense values less than 0.5 were excluded from all conditions. Fold-sense values > 3 for Qb-MBP incubated with antigen and >10 for 1% (v/v) SDS conditions were not considered. These cutoffs were determined heuristically to include the main population of the fold sense values for visualisation purposes and to exclude extreme outliers, such as the appearance or disappearance of a particle which results in unreasonable fold sense values.

Quenchbody library assembly

Quenchbody libraries with evolvable CDRs were assembled using oligonucleotides randomised by trimer phosphoramidite mix (TRIM) as previously described [29] , with the following modifications. CDRs 1, 2 and 3 were assembled by PCR assembly using Vent

polymerase (NEB), with each reaction consisting of 1 x ThermoPol buffer, 5% (v/v) DMSO, dNTPs (0.4 mM), forward and reverse outer primers (1 µM), random TRIM oligonucleotide (50 nM), megaprimer (25 nM), assembly primer (25 nM) and Vent polymerase (2 U), with a final volume to 100 uL. Megaprimers were purchased as 4 nmol ultramers (IDT). Random TRIM oligonucleotides were purchased either from IDT or Ella Biotech GmbH. The CDR 1 reaction consisted of CDR1_c random TRIM oligonucleotide, megaprimer1_c, FW2_C_rev assembly and FW1_c_for and Link1_c_rev outer primers. CDR2 reactions contained Q_CDR2_c randomized oligonucleotide, megaprimer2_c and Link1_c_for and Link2_c_rev outer primers. CDR3 reactions consisted of Q_CDR3_c randomized oligonucleotide, and Link2_c_for and FW4_c_rev outer primers. PCR assembly reactions were: 2 min initial denature at 94 °C, then 30 cycles of 94 °C 30 s, 60 °C 30 s, 72 °C 30 s, then final extension for 5 min at 72 °C. Individual reactions were purified on Macherey Nagel Gel clean-up columns. DNA fragments encoding CDRs 1 and 2 were digested overnight with BsaI-HFv2 and BbsI-HFv2 respectively (NEB). Reactions were cleaned up with Macherey Nagel Gel cleanup columns. DNA products were quantified and ligated in equimolar mixtures. Correct ligation product was gel extracted before PCR amplification with outer oligos FW1_c_for and Link2_c_rev. CDR1+2 fragment was digested with BsaI-HFv2 and CDR3 fragment with BbsI-HFv2 and ligated with T4 ligase. Correct ligation product was gel extracted. BbsI restriction sites were added to the ends of the assembled library with 8 cycles of PCR. PCR products were then digested with BbsI and ligated to an expression vector using T4 ligase.

SNAP display selection

Genes coding for nanobody variants were fused to the N-termius of a SNAP-tag via a Glycine/Serine linker sequence, as part of an expression cassette under the T7 promoter. Genes were fused to dendrimer like DNA structures (DL-DNA), such that each gene displayed eight benzylguanine moieties, as described previously [53]. To assemble nanobody library expression cassettes, we ligated 50 ng of *Bbs*I digested nanobody library to 200 ng of *Bbs*I digested expression vector with complementary overhangs for 1 h at 16 °C. Ligation products were then amplified with "outPCR" primers, containing uracil and overhangs compatible with Thermolabile USER II digestion/ligation (NEB). Following outPCR, DL-DNA were assembled by simultaneous Thermolabile USER II digestion and T4 ligation to DL-DNA structures with compatible cohesive ends. Ligation products were confirmed by agarose gel electrophoresis. The genes were diluted to 125 pM in 30 µL PURExpress cell-free expression mix (NEB) containing 0.06 % pluronic acid (F-127, final concentration) and 1 µL of each disulfide bond enhancer 1 and 2 (NEB #E6820). We used droplet oil consisting of 3M™ Novec™ HFE7500 Engineered Fluid (3M, 7100025016), filtered with a 2 µm cellulose filter (VWR, #514-0061) and supplemented with 2 % fluorinated surfactant FluoSurf neat (Emulseo, #1903) for droplet emulsification. For emulsification, 0.4 mL of droplet oil was loaded into a 1 mL Luer Lock syringe, and the cell free expression mixture layered on-top. A sec 1 mL syringe filled with 0.8 mL of droplet oil connected to a 5 µm hydrophobic membrane pumping device supplied by Shirasu Porous Glass (SPG) (#PC05U). The oil phase was pushed through the SPG membrane until the oil phase was level with the open side. The syringe containing the cell-free expression mix was then connected to the SPG membrane, and the mixture emulsified by repeatedly

alternating the mixture from one syringe to the next, for a total of 10 rapid extrusions through the membrane. The emulsification process produces monodisperse droplets with volumes in the fL range. At ≈ 125 pM in PURExpress cell free expression mix, droplet loading is 0.1 genes per droplet. The emulsion was then transferred into a new 1.5 mL tube and incubated at 37 °C for 4 h, then at 4°C overnight in an Eppendorf thermomixer. To break the emulsion, excess HFE oil was removed by aspirating with a 23G needle from the bottom of the tube, and Perfluoro-1-Octanol (Sigma-Aldrich/Merck, #370533) was added to the tube in 1:1 ratio with the emulsion volume. After vortexing for 15 sec, the tubes were centrifuged at 13,000 rpm for 1 min, and the aqueous phase was recovered in a clean tube. The recovered emulsion was diluted in 5 x Recovery and Binding Buffer (RBB; 40 mM Tris-HCl, pH 7.4, 10 mM EDTA, 1 mM dithiothreitol, 0.5% Tween-20, and 10 uM BG-mPEG12). Magnetic beads displaying recombinant IL-6 protein (BioLegend #570806) were prepared by washing 70 uL of Tosyl-activated M-280 magnetic dynabeads (ThermoFisher #14203), 3 x with 1 mL of PBS for 5 min. IL6 binding buffer was prepared by diluting 10 µg of IL-6 in PBS to a total volume of 75 uL. Beads were coupled to 70 uL of IL6 binding buffer by incubating overnight with end-over-end mixing at 37°C. The quantity of IL-6 bound to beads was determined by absorbance spectroscopy of pre- and post-binding solutions on a nanodrop at A280. Following binding, beads were washed 1 x with 1 mL PBS, then with 1 mL 50 mM Tris-HCl (pH 7.5), 0.5 % Tween-20 for 1 h with end-over-end mixing. Finally beads were washed for 1 h in 1 mL of PBS for 1 h before being washed 1 x and resuspended in 20 µL 50 mM Tris-HCl (pH 7.5), 0.5 % Tween-20. SNAP-display complexes were then selected by affinity panning on IL-6 coated beads (500 nM equivalent IL-6, unless otherwise stated), in a total volume of 75 µL (2 µL of solution was retained for qPCR analysis) for 1 h at room temperature with end-over-end mixing. Selections were washed 5 x in 200 uL of RBB. Bound complexes were then released from the beads by heat shock (20 min at 70 °C) in 15 µL of 50 mM Tris-HCl (pH 7.5), 0.5 % Tween-20 and the selected genes amplified by PCR using Q5® Hot Start polymerase (NEB) using forward primer: GATCACGAAGACATTATGGCGGATCAAGTCCAGCTGGTGGAATCG and reverse primer: GATCACGAAGACATCACCAGAAACGGTAACTTGGGTGCCCTG. PCR reactions were composed of 10 µL Q5 reaction buffer (NEB), 1 µL 10 mM dNTPs (NEB), 2 µL each 10 µM forward and reverse primers, 5 µL elution, 24.5 µL nuclease-free water, 5 µL DMSO, and 0.5 µL Hot-start Q5 high fidelity polymerase. Cycling conditions were 98°C, 2 min, followed by 25–30 cycles of 98°C 30 sec, 60°C 20 sec and 72°C 30 sec. Final extension of 72°C for 2 min. Amplification of recovered genes was verified by agarose gel electrophoresis. Selected genes can then be re-formatted for further rounds of selection.

Results

In silico evaluation of *de novo* quenchbody models

To derive a nanobody-based quenchbody scaffold which could be generally applied to the detection of a broad range of proteins with high performance (i.e., displays a large fluorescence increase upon antigen binding), we initially considered the binding mode of nanobodies with their antigens. It has previously been shown that nanobodies tend to prefer three distinct binding modes known as concave, convex or loop, named for the shape of the nanobody antigen-binding interface [29]. We decided to exclusively use convex-binding nanobodies to provide the most generalisable antigen-recognising surface for fluorophore-tryptophan interaction in nanobody-based quenchbodies, given the favourable compact interface available to the N-terminal fluorophore. Conversely, there were concerns that concave-binding nanobodies might preclude fluorophore access, while loop-binding nanobodies were considered to be too mobile, unstructured or elongated for consistent fluorophore interaction, especially when the naturally-occurring variations in the length of CDR3 are considered across different antigens [54]. Using this constraint, we chose convex-binding nanobodies against maltose-binding protein (MBP) (PDB ID: 5M14) and lysozyme (PDB ID: 1ZVH) as initial scaffolds, due to the availability of high quality (< 2 Å) crystal structures of these nanobodies in complex with their antigens [28, 29]. Given that photoinduced electron transfer is believed to occur over distances ≤ 10 Å [19, 20, 55, 56], we carried out all-atom molecular dynamics (MD) simulations in the absence and presence of antigen, and calculated the distances of the conjugated-TAMRA fluorophore from each of the intrinsic CDR-tryptophans for each nanobody. The W36 framework residue conserved in both nanobodies was deeply buried within the interior of the nanobody and therefore excluded from analysis given its lack of fluorophore accessibility. For the MBP-binding nanobody, which contains three intrinsic tryptophans in the CDRs, TAMRA-tryptophan distances of ≤ 10 Å were observed in the unbound state but not the antigen bound state (Fig 1A). Notably, TAMRA-tryptophan distances of ≤ 10 Å were weakly populated for W101 and strongly populated for W110 and W115 (Fig S1A), suggesting successful albeit variable quenching was possible by all CDR-tryptophans in the unbound state. The average simulation time TAMRA spent ≤ 10 Å from any of the three intrinsic tryptophans was further calculated as 70.7 ± 18.7% in the unbound state and 0.1 ± 0.2% in the antigen-bound state (Table S1). Comparatively, the lysozyme-binding nanobody had two tryptophans in the CDRs (W103 and W115) that could act as potential quenchers, with TAMRA-tryptophan distances of ≤ 10 Å observed for both the unbound and antigen-bound state (Fig 1B). TAMRA-tryptophan distances of ≤ 10 were more strongly populated in the antigen bound state for W103 but not W115 (Fig S1B). Correspondingly, the average simulation time TAMRA spent ≤ 10 Å from any of the CDR-tryptophans in the lysozyme-binding nanobody was calculated as 37.3 ± 24.1 % in the unbound state and 5.9 ± 6.1% in the antigen-bound state (Table S2). Taken together, the results suggest that both nanobodies are suitable candidates for conversion into quenchbodies, although the MBP-binding quenchbody had superior TAMRA-tryptophan interactions *in silico*. Using the MBP-binding nanobody as an example, a model for the quenchbody mechanism is presented, showing the conjugated fluorophore (TAMRA)

quenched by intrinsic tryptophans (W101, W110 and W115) from the CDRs at the top of the nanobody in the unbound native unbound state (Fig 1C). Upon antigen binding to the nanobody CDRs, TAMRA is sterically occluded from W101, W110 and W115, and dequenching occurs, leading to an increase in fluorescence intensity of the fluorophore (Fig 1C).

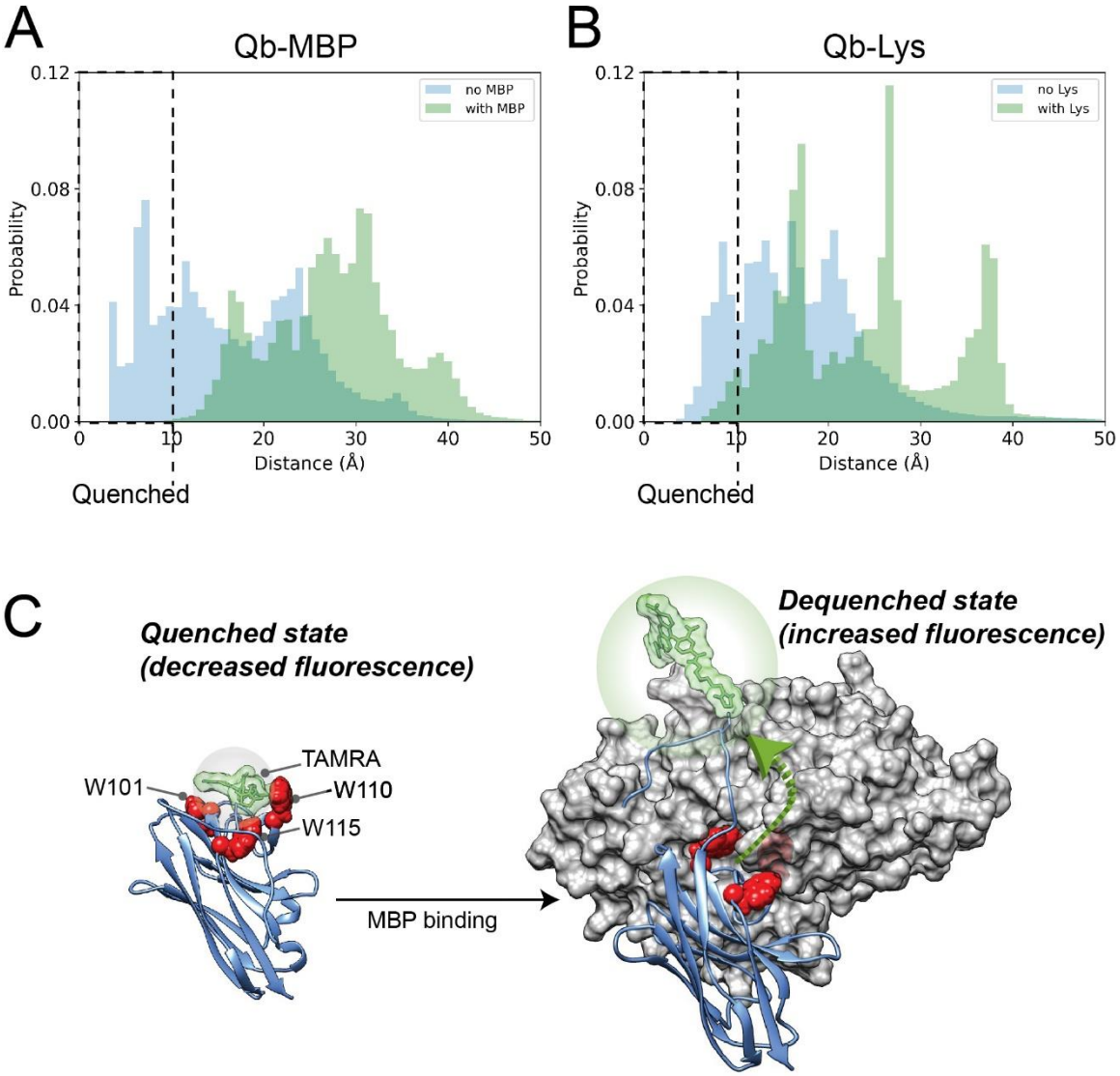

Figure 1. Design and *in silico* modelling of *de novo* quenchbodies. (A) Average normalized distribution histograms illustrating the TAMRA-CDR-tryptophan distances (W101, W110 and W115) derived from MD simulations in the absence (blue) or presence (green) of antigen for the MBP-binding nanobody (PDB ID: 5M14). Individual plots for W101, W110 and W115 are provided (Fig S1A). TAMRA is considered quenched by tryptophan at distances ≤ 10 Å (hatched zone). (B) Average normalized distribution histograms illustrating the TAMRA-CDR-tryptophan distances (W103 and W115) derived from MD simulations in the absence (blue) or presence (green) of antigen for the lysozyme-binding nanobody (PDB ID: 1ZVH). Individual plots for W103 and W115 are provided (Fig S1B). (C) Proposed mechanism of the MBP-binding quenchbody (blue) modelled from PDB ID: 5M14, with N-terminal covalently conjugated TAMRA (green) undergoing quenching due to interaction with the intrinsic CDR-based tryptophans (red spheres). Upon binding to the MBP antigen (grey surface model), TAMRA is sterically occluded from tryptophans (W101, W110 and W115), which is associated with increased fluorescence intensity.

In vitro production and biochemical characterisation of quenchbodies

Sequences encoding MBP-binding and lysozyme-binding nanobodies (based on PDB ID: 5M14 and 1ZVH, respectively) as previously detailed [28, 29], were grafted into an IVTT expression scaffold *in silico*, containing a Cys-tag to enable N-terminal conjugation of a maleimide-TAMRA fluorophore as previously described [21, 22], and a C-terminal Avi-tag, 3 x FLAG tag and 10 x His to facilitate biotinylation and purification procedures (Fig S2A). The full quenchbody peptide sequences are also provided (Fig S2B). Following IVTT protein expression, quenchbodies were captured from the mixture using anti-FLAG magnetic beads, labelled with maleimide-TAMRA, biotinylated, extensively washed and finally eluted from the anti-FLAG magnetic beads using excess FLAG peptide, meaning gene to quenchbody could be rapidly achieved within 2 days. Both the MBP-binding and lysozyme-binding quenchbodies (Qb-MBP and Qb-Lys) appeared as a single band by reducing SDS-PAGE analysis (Fig S2C,D), indicating quenchbodies were of high purity. Purified quenchbodies also showed a single fluorescent band following in-gel fluorescence imaging of reducing SDS-PAGE gels (Fig S2C,D), further supporting successful labelling of quenchbodies with TAMRA. Spectrophotometric analysis of protein:TAMRA suggested stoichiometries were approximately 1:1 quenchbody:TAMRA. Quenchbody-antigen pulldowns were conducted, and reducing SDS-PAGE analysis showed bands consistent with the size of the cognate antigens MBP (~43 kDa) and lysozyme (~15 kDa) alongside the expected size for each of the recombinant quenchbody bands (~21 kDa) (Fig S2C,D). The latter suggested that the quenchbodies were functional and quenchbody-antigen binding had not been affected by N-/C-terminal modifications. We next employed a 384-well plate-based assay and tested the fluorescence fold-increase of quenchbodies in the presence of antigen (fold-sense) or denaturant (fold-quench), with respect to a native quenchbody control. Qb-MBP showed a maximal 1.5 fold-sense at ≥ 100 nM MBP, with statistically significant detection of as low as 4 nM MBP versus the 0 nM MBP control (Tukey's multiple comparisons, $p = 0.0002$) (Fig 2A). In line with earlier *in silico* predictions, a slightly lower 1.3 fold-sense was observed for Qb-Lys at ≥ 1000 nM lysozyme, with statistically significant detection of as low as 1 nM lysozyme (Tukey's multiple comparisons, $p = 0.0002$) (Fig 2B). Upon denaturation of the quenchbodies, a 3.6 fold-quench for Qb-MBP (Fig 2A) and a 2.1-fold-quench for Qb-Lys was observed (Fig 2B). This observation suggested that incomplete dequenching of the fluorophore was occurring in the antigen bound state, implying that the antigen was also quenching the fluorophore. The half-maximum effective concentration (EC_{50}) was calculated as 14 nM for Qb-MBP (Fig 2C) and 7 nM for Qb-Lys (Fig 2D), which was comparable with previously-reported binding affinities for the 5M14 MBP-binding nanobody (K_D = 24 nM)[29] and the 1ZVH lysozyme-binding nanobody (K_D = 60 nM) [28], respectively, suggesting the quenchbody assay is reporting the fraction bound.

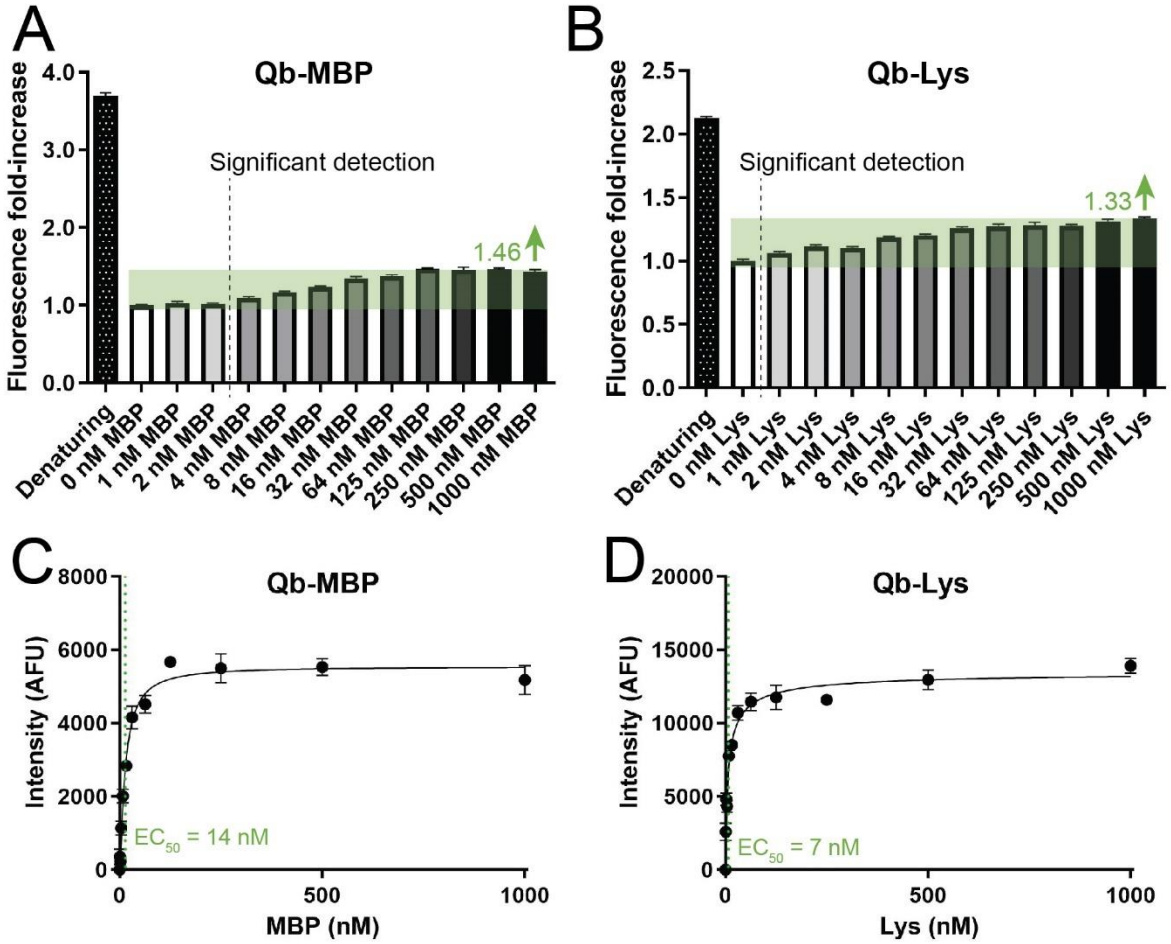

Figure 2. Fluorescence intensity changes in TAMRA-labelled quenchbodies upon antigen binding or denaturation. (A) Qb-MBP or (B) Qb-Lys were incubated (60 min, 25°C) in the presence of 1000, 500, 250, 125, 64, 32, 16, 8, 4, 2, 1, or 0 nM of their cognate antigens, MBP or lysozyme, or in the presence of a denaturant (2% SDS, 5% β-mercaptoethanol). Data are mean ± SD of the TAMRA fluorescence fold-increase relative to the 0 nM antigen native sample (excitation = 535 ± 20 nm and emission = 585 ± 30 nm). The lowest point of statistically significant detection is indicated (Ordinary one-way ANOVA, Tukey's multiple comparisons, $p = 0.002$), with concentrations listed to the left of the hashed line considered to be non-significant ($\alpha = 0.05$). Fluorescence intensity responses of (C) Qb-MBP or (D) Qb-Lys to their cognate antigens was quantified fitted to an equation describing a single site-specific binding mode to derive an EC_{50} as a proxy measure for quenchbody binding affinity (K_D). Data are mean ± SD normalised fluorescence intensity (N.F.I. (AFU)).

Single molecule characterisation of quenchbody performance

Our earlier measurements on different quenchbody variants showed consistently higher values of fold-quench versus fold-sense, suggesting that the quenchbody was not achieving full dequenching in the antigen-bound state. This implies that the antigen could be inter- or intra-molecularly quenching the quenchbody, or a portion of the quenchbody is non-functional. To address these hypotheses and explore the utility of quenchbodies as single molecule biosensors, we investigated the behaviour of individual quenchbody molecules by total internal reflection (TIRF) microscopy. Using Qb-MBP (fold-sense = 1.5, fold-quench = 3.7, earlier bulk measurements), which was biotinylated and immobilised to a neutravidin-functionalised glass coverslip in a microfluidic setup to facilitate buffer exchange and remove the possibility of inter-molecular quenching (Fig 3A), we acquired time-lapse images of Qb-MBP in its native, antigen-bound and denatured state (Fig 3B). Density was controlled to ensure sufficient spacing between particles, while unbound particles were removed by buffer exchange in the microfluidics setup. This allowed for 9,000 ± 1,200 traces (mean ± SD) to be analysed per treatment. The fluorescence of Qb-MBP can still be detected in the absence of antigen or denaturant, and fluorescence is therefore not completely quenched in the unbound state (Fig 3C). An example of the images obtained for single molecule analysis is provided, showing the fluorescent intensity increase following addition of denaturation buffer at 10 frames (Fig 3C). The ratio of the mean intensity before/after addition of buffer, MBP or denaturant was subsequently quantified to derive the fluorescence fold-increase for each particle. For quenchbody particles exchanged with buffer absent of antigen (0 nM MBP) there is a mean fold-sense of approximately 1.1 (Fig 3D, blue). Quenchbody particles exchanged with excess antigen (250 nM MBP) appeared to be only partially responding with a mean fold-sense of 1.2 observed (Fig 3D, orange). Quenchbody particles exchanged with denaturant were widely distributed in their fluorescent response, although a much higher response with a mean fold-quench of 4.6 observed (Fig 3D, green). Taken together, the single molecule measurements indicate that the consistently lower fold-sense vs fold-quench of quenchbodies is likely to be caused by the protein antigen quenching the fluorophore in the antigen-bound state, and/or the existence of a non-functional but labelled population of quenchbodies which are incapable of binding MBP.

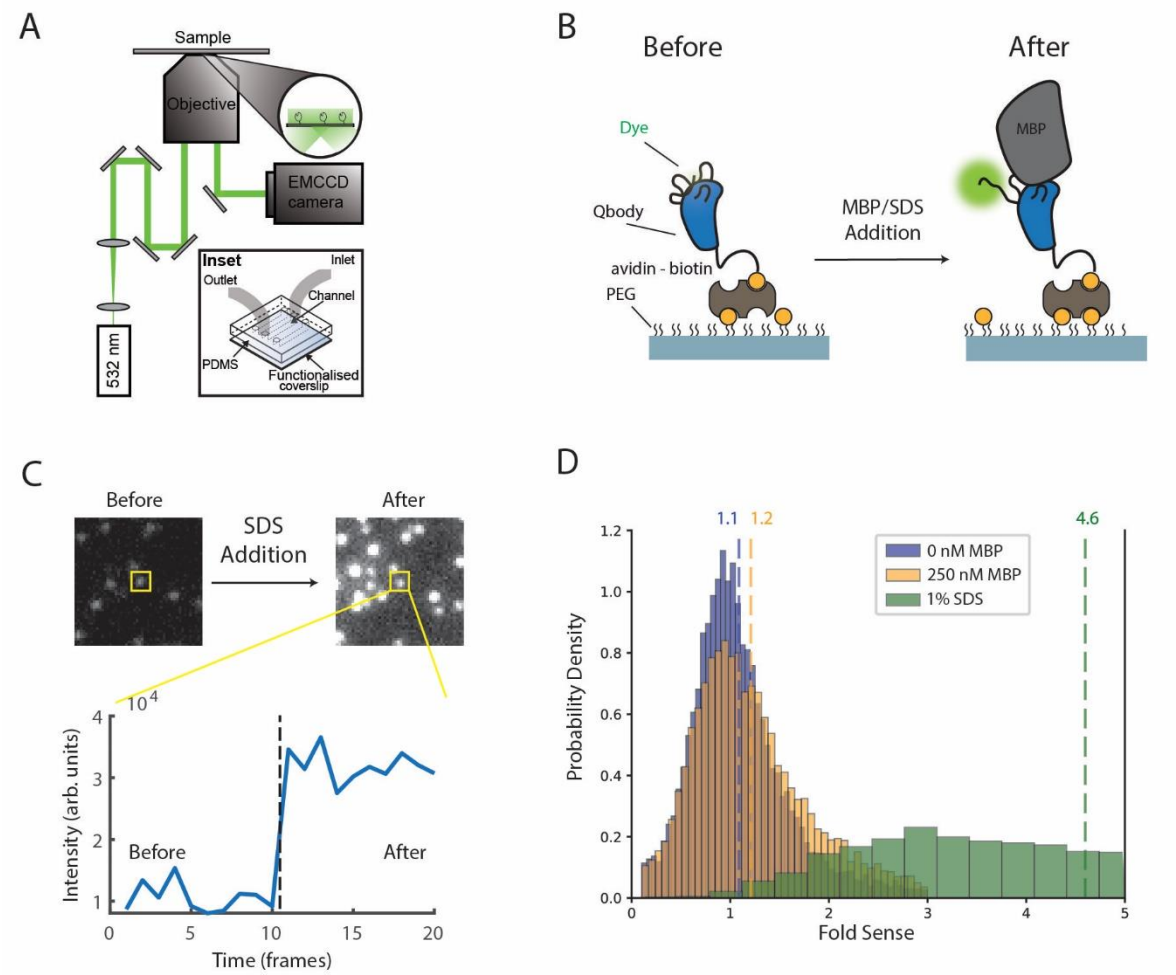

Figure 3. Single-molecule studies of fluorescent intensity changes in Qb-MBP upon antigen binding or denaturation. (A) Schematic of the TIRF microscope and microfluidics device used to collect images. (B) Cartoon representation of the Qb-MBP single-molecule assay. (C) Sub-average of images collected before and after denaturant addition (1% SDS) alongside an example trajectory of a single particle highlighted by yellow box. The dashed vertical line denotes incubation with denaturant. (D) Probability density functions of fold sense value of individual particles in 0 nM MBP (negative control, blue), 250 nM MBP (saturating concentration, orange) and 1% SDS (denaturation control, green) along with corresponding mean values denoted by dashed lines and numbers of the corresponding colour.

CDR-tryptophans underpin the quenchbody sensing mechanism

Photoinduced electron transfer (PET) from intrinsic quenchbody tryptophans to the fluorophore has previously been identified as the key quenching mechanism [15-18]. However, there are not clear guidelines for where tryptophans are best placed in nanobody-based quenchbodies, especially when aiming for generalisable detection of different antigens. In Qb-Lys, of the three tryptophans, W36, 103 and 115, only W103 and 115 are in the CDRs, and only W103 appears to interface directly with lysozyme (Fig 4A). W115 is on the surface of Qb-Lys but does not interface with lysozyme (Fig 4A), unlike W115 in Qb-MBP which interacts with MBP, and can, therefore, potentially quench in both the apo- and antigen-bound state due to its proximity to the N-terminus, as inferred from earlier *in silico* modelling (Fig 1 and Table S2). The third tryptophan, W36 is deeply buried within the beta-sheet-rich barrel of the nanobody (Fig 4A), and is therefore unlikely to quench TAMRA in either the apo- or antigen-bound states. The variants W103Y, W115Y and W103Y/W115Y were subsequently created to test the importance of these tryptophans in the quenching mechanism. Tyrosine substitution was chosen to mimic the biochemical properties of tryptophan residues to minimally disturb Qb-Lys structure and function in accordance with FoldX predictions (Table S3) [47]. In the presence of 500 nM lysozyme, the W115Y mutant had near identical performance to the WT control, indicating that this tryptophan was unlikely to be important in the quenching mechanism (Fig 4B). There was no significant increase in fold-sense of W103Y in the presence of 500 nM lysozyme (Fig 4B). Pulldown assays to assess binding of lysozyme showed that W115Y had equivalent binding compared to WT, while W103Y had reduced binding to lysozyme (Fig S3), which was to be expected given W103Y is a residue directly involved in lysozyme binding. Average solvent accessible surface areas of intrinsic tryptophans sampled from MD simulations of the apo- and antigen-bound states showed W103 in Qb-Lys and W101, W110, and W115 in Qb-MBP had markedly reduced solvent accessibility in the antigen-bound versus unbound state (Table S4), which appeared to be caused by the antigen sterically blocking the tryptophans from accessing solvent. Taken together, these data suggest that CDR-based tryptophans which directly interface with antigens are the most important quenchbody tryptophans for quenching and subsequently becoming dequenched upon antigen binding, resulting in the measured fluorescence increase in the antigen-bound state.

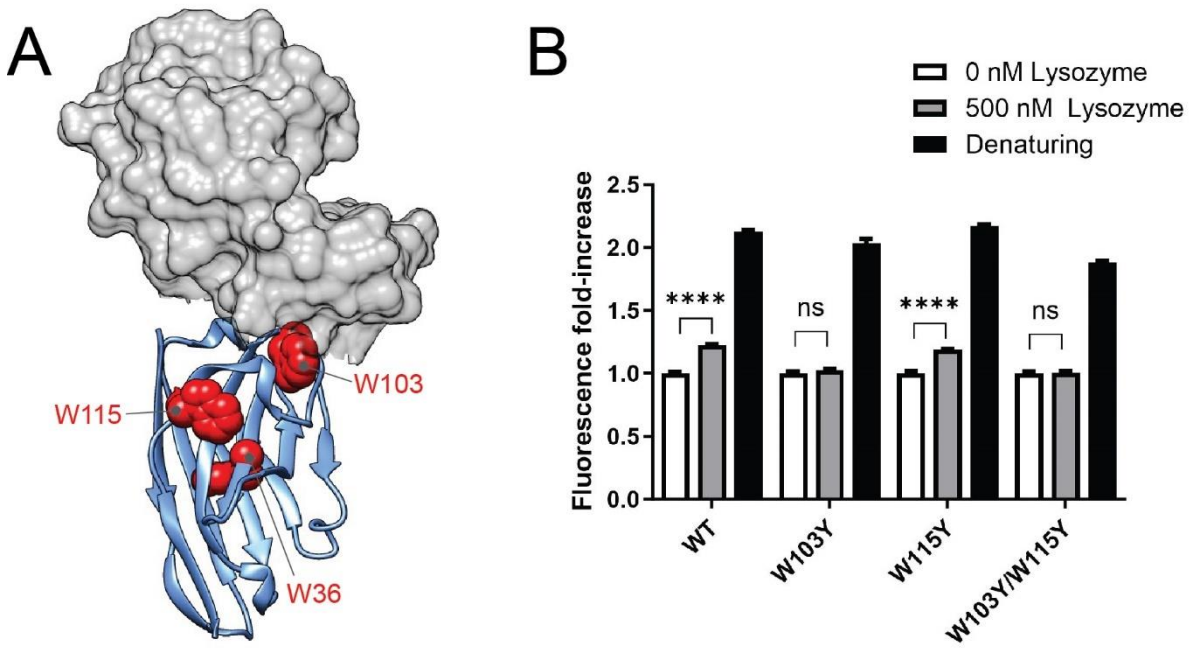

Figure 4. Tryptophan-mediated quenching in Qb-Lys. (A) Model of Qb-Lys (blue) highlighting all intrinsic tryptophans (red spheres), in complex with lysozyme (grey surface model), based on PDB ID: 1ZVH. (B) WT, W103Y, W115Y or W103Y/W115Y lysozyme quenchbody variants were incubated (60 min, 25°C) in the absence or presence of 500 nM lysozyme or denaturant (2% SDS/5% β-mercaptoethanol). Data are mean ± SD of the TAMRA fluorescence (excitation = 535 ± 20 nm and emission = 585 ± 30 nm) fold-increase when normalised to the fluorescence signal in the 0 nM lysozyme condition. Ordinary one-way ANOVA with Tukey's multiple comparisons shows significant (**** = $p < 0.0001$) or non-significant (ns) differences.

Based on this information, we subsequently attempted to improve the fold-sense of Qb-Lys by performing the reverse mutation and substituting CDR-tyrosines with tryptophans (Y27W, Y104W and Y110W). MD simulations showed that Y27W, Y104W and Y110W could each contribute to the quenching of TAMRA in the unbound state for approximately 50% of the time but for only approximately 5% of the time in the antigen-bound state (Fig S4 and Table S5), while FoldX predicted Y27W, Y104W and Y110W would be suitable for maintaining protein stability and antigen binding (Table S6) [47]. We therefore produced single, pairwise, and triple Y27W, Y104W and Y110W mutants of Qb-Lys. All tryptophan substitutions did not appear to affect antigen binding as measured by pulldown assay (Fig S5) and improved the fold-quench of the quenchbody (Table 1). However, the Y110W single mutation emerged as the best for maximising fold-sense (Y110W = 1.7, WT = 1.3), while single mutations of Y27W or Y104W were equivalent to WT (Table 1). To test the generalisability of this strategy to other quenchbodies, we next targeted Qb-MBP for substituting CDR-tyrosines with tryptophans. A Y114W single mutant was first produced as it was considered potentially redundant based on its proximity to existing W110 and W115. The Y114W mutant retained its binding affinity and slightly improved the quenchbody fold-sense to 1.6 (the WT is 1.5) (Table 1). Therefore, the Y114W mutant was kept constant in further single, pairwise and triple mutations (Table 1). The Y59W/Y114W mutant had an improved fold-sense of 1.9, suggesting a large improvement due to Y59W. For all other mutants fold-sense was lower than the Y114W mutant, and in some cases lower than WT (Table 1), which was typically a result of loss of binding to the antigen as observed by pulldown assay (Fig S6). Furthermore, a triple knockout of the intrinsic tryptophans, W101A/W110A/W115A, produced a fold-quench of 1.5, compared to 3.6 for WT (Table 1), supporting that amino acids other than tryptophan may be contributing, albeit less powerfully, to the quenching effect, such as tyrosine, phenylalanine, methionine, and/or histidine [57, 58]. Interestingly, the fold-quench of all Y to W mutants was unchanged or increased, but this did not always correlate with increases in the fold-sense of the quenchbody, suggesting a potential for diminishing returns from mass tryptophan addition. Based on this information, tryptophans which contributed favourably to fold-sense for building a generalisable quenchbody scaffold were W59, W101, W103, W110, and W115.

Table 1. Tryptophan substitution screening to inform design of improved MBP and lysozyme quenchbody variants.

Mutant	Fold-sense[1]	Fold-Quench[2]	Binding[3]
1ZVH scaffold (Qb-Lys)			
WT	1.33	2.1	++
Y27W	1.30	2.76	++
Y104W	1.35	2.79	++
Y110W	1.65	3.28	++
Y27W/Y104W	1.41	3.24	++
Y27W/Y110W	1.63	3.62	++
Y104W/Y110W	1.54	4.00	++
Y27W/Y104W/Y110W	1.42	4.41	++
5M14 scaffold (Qb-MBP)			
WT	1.46	3.6	++
Y114W	1.64	3.55	++
Y33W/Y114W	1.06	6.12	+
Y54W/Y114W	1.57	11.90	+
Y59W/Y114W	1.88	10.56	++
Y33W/Y54W/Y114W	1.07	10.10	-
Y33W/Y59W/Y114W	1.17	13.87	+
Y54W/Y59W/Y114W	1.31	16.41	+
Y33W/Y54W/Y59W/Y114W	1.09	17.86	-
W101A/W110A/W115A	1.00	1.53	-

[1]Fold-sense is the fluorescence fold-increase of the quenchbody in the presence of antigen, relative to the fluorescence of the quenchbody alone

[2]Fold-quench is the fluorescence fold-increase of the quenchbody in the presence of denaturant, relative to the fluorescence of the quenchbody alone

[3]Binding is a semi-quantitative measure reporting the effect the mutation had on the binding affinity of the quenchbody, as assessed by a reducing SDS-PAGE pulldown assay detailed in Supplementary Materials (++ similar binding to WT, + less binding than WT, - negligible binding)

In vitro evolution of CDR-tryptophan quenchbodies for IL6 detection

To assess whether CDRs enriched with tryptophan residues could be used to evolve nanobody-based quenchbodies against a bespoke protein target (human IL6, accession # NM_000600), we first assembled a synthetic nanobody library encoding CDRs randomised by TRIM oligonucleotides, in line with a previous strategy [29]. However, position 59 in CDR2, and positions 101, 103, 110 and 115 in CDR3, encoded tryptophan to produce quenchbodies with superior fold-sense (Fig S7A). Naive libraries were assembled by PCR randomisation of CDRs 1, 2 and 3 (Fig S7B), and correct product sizes were confirmed by agarose gel electrophoresis (Fig S7C). We next selected our synthetic quenchbody library in duplicate with IL6-coated magnetic beads using 5 rounds of modified SNAP-display [59] (Fig S7D), with a parallel control of blank beads to control for non-specific binding of nanobodies to the matrix (1 round accomplished over 2 days). Nanobody sequences selected by SNAP-display were tracked by Illumina NGS on a MiSeq instrument (Fig 5A), producing on average 5.4×10^5 reads per library per round. An average of 63 % of reads per round passed quality filtering and encoded a nanobody sequence, which increased from 59 % in round 1, to an average of 71 % (± 2.6 % SD) by round 5 (Fig S8A,B and C), indicating a purifying selection on correctly assembled nanobody genes. Finally, we extracted the top twelve hits from these screens based on their abundance in round 5 (in either selection 1 or 2), removing sequences that were enriched on blank beads (Fig S8D, E and F). Nanobody sequences corresponding to the top 12 hits were each grafted into the IVTT-expression cassette containing quenchbody elements and purified *in vitro* (Fig S9A and D). Screening of IL6 quenchbodies in a fluorescence plate assay showed 3 out of 12 responders, with fold-sense of 1.9, 1.1 and 1.5, respectively, for Qb-IL6-1, Qb-IL6-2, and Qb-IL6-10 upon incubation with 500 nM IL6 (Fig 5B). Further characterisation indicated a maximal 2.2-fold increase in fluorescence intensity for Qb-IL6-1 at ≥ 4,000 nM IL6, with EC_{50} = 185 nM (Fig 5C). In comparison, a maximal 2.0-fold increase in fluorescence intensity was observed for Qb-IL6-10 at ≥ 8,000 nM IL6, with EC_{50} = 1,113 nM (Fig 5D), while an EC_{50} could not be derived for Qb-IL6-2. We sought to increase the affinity of IL6 binding quenchbodies by introducing single randomised codons into each CDRs 1, 2 and 3 for Qb-IL6-1, 2 and 10 (Fig S10A). Furthermore, we constructed a library from oligopools, in which all of the CDRs from Qb-IL6-1, 2 and 10 were mixed (Fig S10B), producing clones corresponding to each parent quenchbody, as well as hybrid library members exhibiting mixed CDRs from Qb-IL6-1, 2 and 10. We performed three rounds of selection on against 500, 50, 5 and 0.5 nM IL6, and blank bead controls, and tracked selections by Illumina NGS on a MiSeq instrument (Fig 5E; Fig S10C). Enrichment scores were determined by dividing the relative abundance in round three with the abundance of blank bead controls. Hits were selected by filtering for sequences with an enrichment score > 200 across IL6 selections and no enrichment in the blank bead selection. We further filtered this list for low abundance sequences by removing sequences with reads from all screens with enrichment score ≤ 150. The top 4 hits were selected from each IL6 screen. An additional 8 hits were picked from the 0.5 nM IL-6 selection. These 8 hits exhibit an enrichment score > 100 and read counts > 60 while showing no enrichment in the blank beads. Affinity-matured nanobody sequences selected as the top 24 hits were clustered according to their CDR3, with 15 corresponding to variants of Qb-IL6-1, 7 for Qb-IL6-2 and 2 for Qb-IL6-10 (Fig S10D). Hits corresponding to Qb-

IL6-1 and Qb-IL6-10 parental CDR3 sequences were all hybrid genes, with 65 % of CDR 1 and CDR 2 elements derived from Qb-IL6-2. CDRs 1, 2 and 3 in hits from Qb-IL6-2 were derived from the parental sequence. We then grafted into the IVTT-expression cassette containing quenchbody elements for production *in vitro* (Fig S9B,C, E and F). Screening of the affinity-matured IL6 quenchbodies in a fluorescence plate assay revealed 11/24 quenchbodies had fold-sense between 2.4–1.5, with EC_{50} values between 436–20 nM (Fig S11), representing an increase in fold-sense and affinity from parent Qb-IL6-1, Qb-IL6-2 and Qb-IL6-10 quenchbodies (Fig 5F). A group of 5/7 hybrid IL6 quenchbodies (parent lineage: CDR1 = Qb-IL6-1, CDR2 = Qb-IL6-2, and CDR3 = Qb-IL6-1) all showed fold-sense of > 2. In some cases, lack of fold-sense response from some quenchbodies was observed to correlate with poor nanobody expression or structural heterogeneity as observed by reducing SDS-PAGE analyses (Fig S9). Notably, fold-quench measurements for all candidate anti-IL6 quenchbodies were larger (Fig S11G; most with fold-quench ≥ 7), compared to that seen with the WT Qb-MBP and Qb-Lys containing fewer tryptophan residues (fold-quench ≤ 4), suggesting W59, W101, W103, W110, and W115 were contributing to quenching capacity in the unbound state. Taken together, the data suggest that our CDR-tryptophan-optimised synthetic nanobody scaffold is suited to the discovery of generalisable quenchbodies with high fluorescence intensity performance when detecting future protein targets of interest.

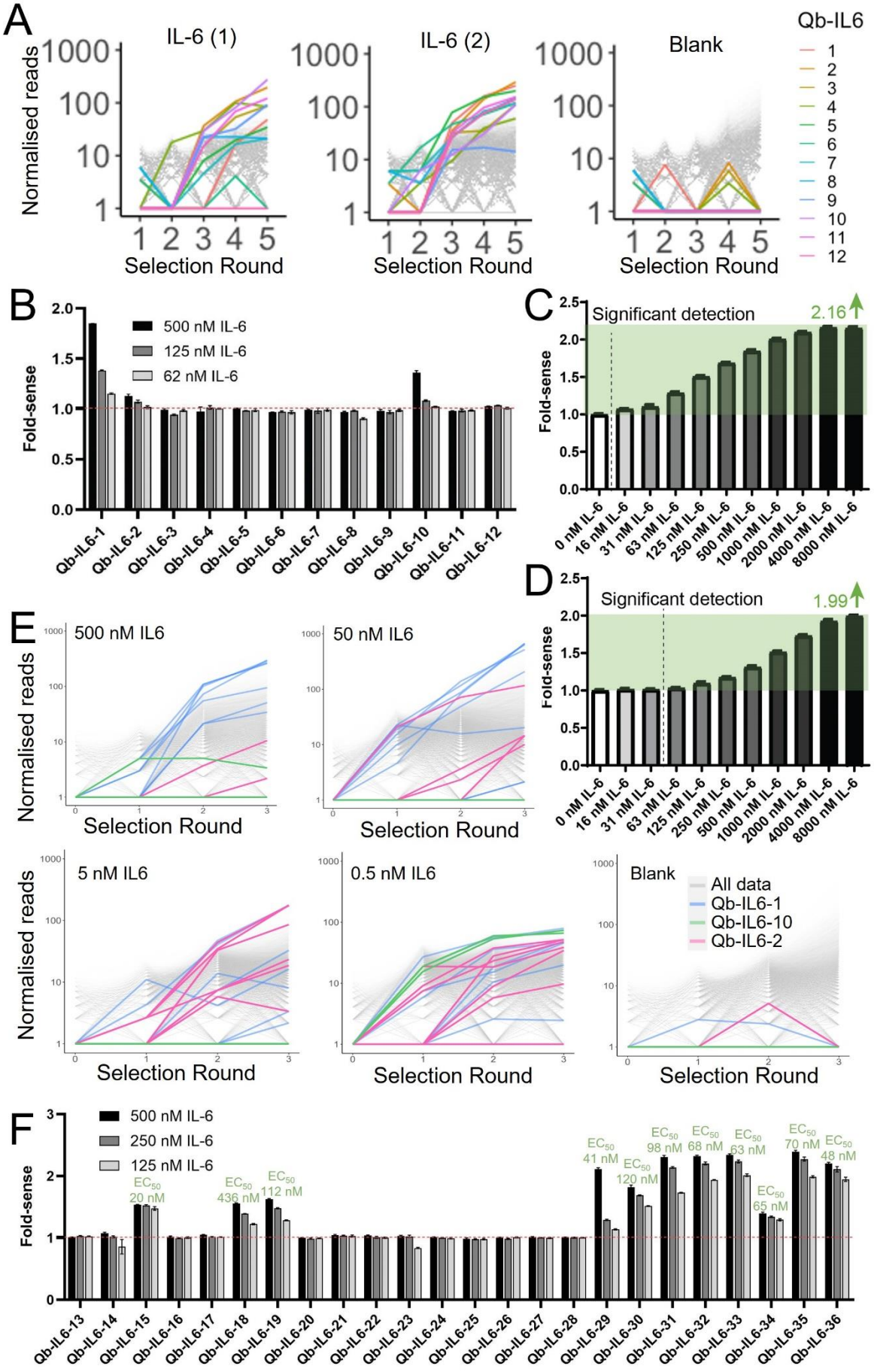
A
IL-6 (1)
IL-6 (2)
Blank
Qb-IL6
Normalised reads
Selection Round
B
500 nM IL-6
125 nM IL-6
62 nM IL-6
Fold-sense
C
Significant detection
2.16
D
Significant detection
1.99
E
500 nM IL6
50 nM IL6
5 nM IL6
0.5 nM IL6
Blank
All data
Qb-IL6-1
Qb-IL6-10
Qb-IL6-2
F
500 nM IL-6
250 nM IL-6
125 nM IL-6
EC50 20 nM
EC50 436 nM
EC50 112 nM
EC50 41 nM
EC50 120 nM
EC50 98 nM
EC50 68 nM
EC50 63 nM
EC50 65 nM
EC50 70 nM
EC50 48 nM

Figure 5. Evolution of novel CDR-tryptophan quenchbodies and subsequent characterisation of IL6-induced fluorescence intensity changes. (A) Enrichment curves of quenchbody hits. Lines show normalised read counts over rounds 1–5 selecting for IL6 binding over 2 technical replicates (left, center) and blank beads (right). Each hit is indicated as a separate colour. (B) Quenchbodies evolved against IL6 (Qb-IL6-1–12) were screened in a fluorescence plate assay after incubation (60 min, 25°C) with 500, 125, or 62 nM IL6. All data are mean ± SD of the TAMRA fluorescence fold-increase when normalised to the signal with 0 nM IL6 (excitation = 535 ± 20 nm and emission = 585 ± 30 nm). The red hashed line indicates no response to antigen. (C) Qb-IL6-1 and (D) Qb-IL6-10 were analysed in a fluorescence plate assay as above, except in the presence of 8,000, 4,000, 1,000, 500, 250, 125, 64, 32, 16, or 0 nM of IL6. The lowest point of statistically significant detection is indicated (Ordinary one-way ANOVA, Tukey's multiple comparisons, $p < 0.0001$), with concentrations listed to the left of the hashed line considered to be non-significant ($\alpha = 0.05$). (E) Enrichment curves of affinity maturation conducted on initial quenchbody hits Qb-IL6-1, Qb-IL6-2 and Qb-IL6-10, assembled as a combinatorial library. Lines show normalised read counts over rounds 1–3 for selection against of IL6 (concentration A = 500 nM, B = 50 nM, C = 5 nM, D = 0.5 nM), or blank beads (0 nM). Qb-IL6-1 = blue, Qb-IL6-2 = magenta and Qb-IL6-10 = green. (F) Affinity matured quenchbodies evolved against IL6 (Qb-IL6-13–36) were screened in a fluorescence plate assay as above except with 500, 250, or 125 nM IL6.

Discussion

Through a combination of *in silico* modelling, biochemical characterisation, and targeted mutational screening, we developed synthetic nanobody libraries containing conserved CDR-tryptophans that can be selected and optimised via *in vitro* evolution using SNAP-display to rapidly produce *in vitro* nanobody-based quenchbodies that display superior fluorescence increases of 1.5–2.4 (fold-sense) when recognising proteins of interest in a homogenous immunoassay. This is a marked improvement over the fold-sense of 1.3–1.5 obtained for nanobodies against MBP and lysozyme which we engineered into quenchbodies in the present study, and fluorescence fold-increases of 1.1–1.7 reported for other nanobody-based quenchbodies against proteins including albumin [15, 22], claudin [25], human epidermal growth factor receptor-2 (HER2) [26], and hemagglutinin [27]. Furthermore, the tryptophan-optimised quenchbody is nanobody-based, which holds several advantages over more common scFv-based or Fab-based quenchbodies, including higher stability, tolerance to mutation and ease of production [16]. This work therefore demonstrates a generalisable strategy for the rapid production of nanobody-based quenchbody biosensors with high fluorescence performance against proteins of interest within 2–3 weeks. Given that we were able to successfully evolve high-performing quenchbodies against IL6, a master mediator of human inflammation [60], these tryptophan-optimised quenchbodies hold great promise for clinical, diagnostic, or therapeutic applications, such as the detection of IL6 and potentially other biomarkers in biological fluids.

This work also provided unique insights into the quenching mechanism involving key tryptophan residues of nanobody-based quenchbodies. In scFv and Fab-based quenchbodies semi-conserved tryptophan residues in the VH + VL interface (not in the CDRs), quench the flexible N-terminal fluorophore in the unbound state, with antigen binding causing allosteric displacement of the fluorophore from the interface through a conformational change in the scFv [15, 61]. Our study supports a different mechanism for nanobody-based quenchbodies, whereby CDR-tryptophan residues that directly interface with the protein antigen are the most important for TAMRA dequenching to detect the antigen-bound state via an increase in fluorescence (Figure 4). This is similar to previous tryptophan-substitution experiments involving a nanobody-based quenchbody for methotrexate, which revealed that the methotrexate-contacting W34F substitution located in CDR1 as a key quenching residue for methotrexate detection [21]. However, in the latter case methotrexate binding translocated W34 of CDR1 away from the fluorophore via a conformational change in the antigen-bound state [21], which is different to the mechanism of the present quenchbody scaffold which contains a convex-binding surface for generalised dequenching in the antigen-bound state. As such, CDR1-W34 quenchbodies may be more useful for recognising smaller antigens (haptens) which cause molecular displacement of CDR1, whereas convex-binding quenchbodies from the present work may be more useful for recognising larger antigens, such as proteins, which block the convex-surface formed by CDR1, 2 and 3.

Although IL6 quenchbodies that performed well were evolved in the present study, poorly performing quenchbodies were also obtained. High-resolution experimental structures of the quenchbody-IL6 complexes will likely be key for determining why some quenchbodies were

good responders, whereas others failed to respond. We speculate that some IL6 quenchbodies failed to respond because IL 6 is a relatively small antigen, and depending on the mode of binding, it is possible that tryptophans are accessible to the fluorophore at the antigen-quenchbody interface if IL6 does not completely envelope the convex-binding surface of the quenchbodies. Therefore, evolution of convex-binding nanobodies containing conserved CDR-tryptophans to bind large protein targets which completely occupy the convex-binding surface might lead to high success rates for future quenchbody development. It is also possible that the bound antigen may quench the N-terminal fluorophore of the quenchbody given its proximity, especially if the bound antigen has surface-exposed amino acids capable of quenching the fluorophore. The latter may in part explain why the fluorescence fold increase (fold-sense) observed for quenchbodies binding proteins is generally lower (1.1–1.7-fold) [15, 22, 25-27], compared to some extreme cases observed for the fluorescence fold-increase of quenchbodies against peptides (< 9.6-fold) [62, 63] and small molecules (< 6.0-fold) [21, 64], which may lack quenching amino acids such as tryptophan. The discrepancy between fold-sense and fold-quench values in bulk spectrofluorometer plate-screening (Table 1), as well as our single molecule observations (Fig 3), further support the bound protein antigen may be quenching the fluorophore, or there is a sub-population of labelled nanobodies which do not function as quenchbodies due to non-specific labelling or failure to bind the antigen. Although quenchbodies currently perform well for the detection of smaller molecular antigens, protein antigens remain a challenging but worthy goal for quenchbody development

There are numerous ways to potentially improve the antigen-dependent fluorescence fold-increase of quenchbodies without modification of tryptophan residues. For example, substituting TAMRA with similar dyes ATTO520 or rhodamine 6G can lead to improvements [65, 66], although this is not a panacea and seems to vary depending on the quenchbody-antigen pair [21, 65]. In addition, modification of the N-terminal amino-acid linker length where the fluorophore attaches, or changing the length of the C spacer in the fluorophore itself (e.g. C0 – 6), are other ways of potentially improving quenchbody performance, provided it can improve the interaction of the fluorophore with quenching residues in the unbound state but not the antigen-bound state [15, 21, 63, 65]. Furthermore, double-labelling quenchbodies with two fluorophores at positions that allow dye-dye H-dimer formation, causing additional dye quenching in the unbound state but not the antigen bound state, can lead to further improvements, and are known as “ultra-quenchbodies” [27, 67, 68]. These ultra-quenchbodies exhibit fluorescence fold-increases as high as 50-fold in some cases, but this design can so far only be applied to scFv or Fab [68], with no nanobody versions currently existing. Given disparity in fold-quench and fold-sense measurements indicated that intra-molecular quenching by the antigen is also likely occurring, leading to reduced fold-sense performance of the quenchbody, incorporation of an orthogonal quencher (e.g. quencher not based on natural amino acid side chains) into the CDRs, potentially via unnatural amino acid incorporation or bioconjugation, could potentially lead to quenchbodies with huge improvements in fold-sense. Ultimately, it would be interesting to investigate each of these as potential strategies of improving the current tryptophan-optimised quenchbody and will form the subject of ongoing investigations.

Considering IL6 is present in picomolar quantities (5.2 pg/mL in the blood of healthy individuals [69]), the diagnostic usefulness of the IL6 quenchbodies generated in this study (top EC_{50} = 20 nM) is currently limited to scenarios where the IL6 concentration is massively raised, such as septic conditions (1600 pg/mL [70]), or where IL6 is pre-enriched. Affinity maturation of top performing IL6 quenchbodies through additional evolution and screening may potentially produce quenchbodies with sub-nanomolar affinity for IL6 and therefore raise the efficacy of detection close to the requirements for diagnostic detection of IL6 in blood plasma. In addition, a "double quenchbody" approach could be applied to increase the affinity, as it has been previously shown that dimeric ultra-high affinity nanobodies can achieve binding affinities as low as ~0.03 nM [71]. Ultimately, work which aims to improve the sensitivity of quenchbodies is of great interest for generating a viable homogenous immunoassay which could eventually replace ELISA for detection of low abundant analytes, such as IL6. The ease of generation of quenchbodies, coupled with their entirely synthetic evolvability and rapid production within just a few weeks, supports the continued development of the quenchbody assay.

Supplementary Materials – Figures

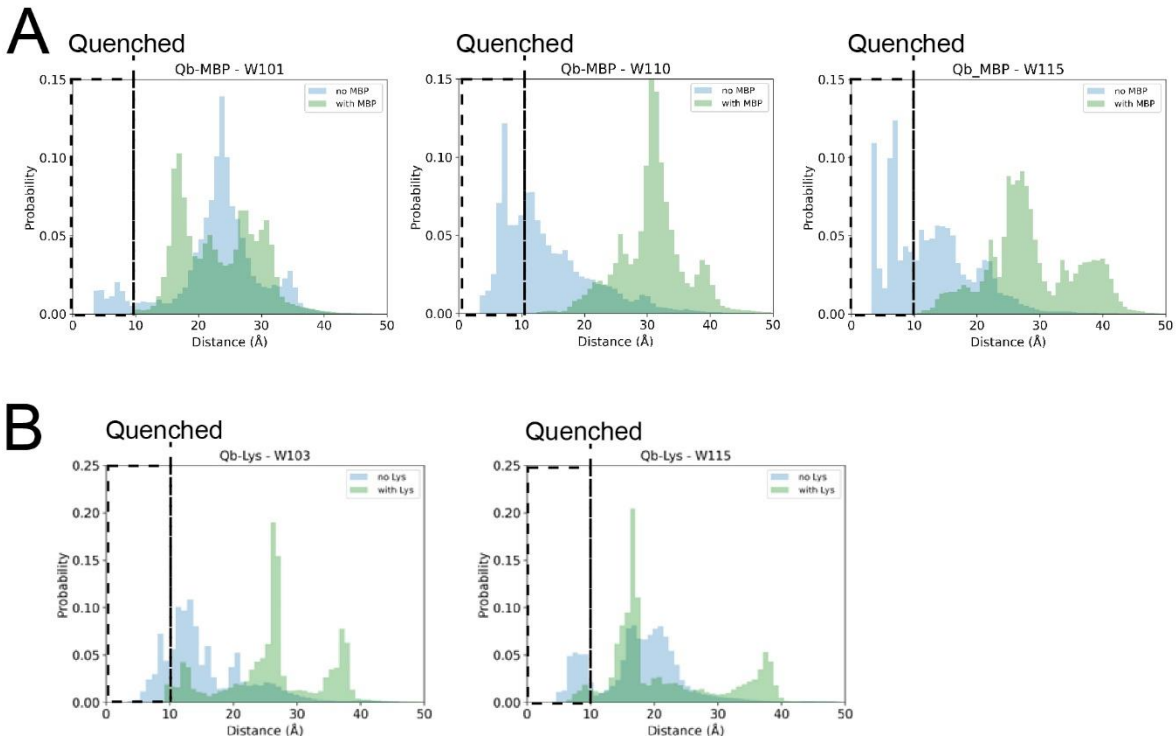

Figure S1. Design and *in silico* modelling of *de novo* quenchbodies. (A) Normalized distribution histograms illustrating the TAMRA-CDR-tryptophan distances (W101, W110 and W115) derived from MD simulations in the absence (blue) or presence (green) of antigen for the MBP-binding nanobody (PDB ID: 5M14). TAMRA is considered quenched by tryptophan at distances ≤ 10 Å (hatched zone). (B) Normalized distribution histograms illustrating the TAMRA-CDR-tryptophan distances (W103 and W115) derived from MD simulations in the absence (blue) or presence (green) of antigen for the lysozyme-binding nanobody (PDB ID: 1ZVH).

A

B

>Qb-MBP

MSKQIEVNYCSNETGSQVQLVESGGGSVQAGGSLRLSCAASGQIEHIGYLGWFRQAPGKEREGVAALITY
TGHTYYADSVKGRFTVSLDNAKNTVYLQMNSLKPEDTALYYCAAAEWGSQSPLTQWFYRYWGQGTQVT
VSGSGLNDIFEAQKIEWHEDYKDHDGDYKDHDIDYKDDDDKHHHHHHHHHH

>Qb-Lys

MSKQIEVNYCSNETGSDVQLVESGGGSVQAGGSLRLSCAASGYIASINYLGWFRQAPGKEREGVAAVSPA
GGTPYYADSVKGRFTVSLDNAENTVYLQMNSLKPEDTALYYCAAARQGWYIPLNSYGYNYWGQGTQVT
VSSRGRGSGLNDIFEAQKIEWHEDYKDHDGDYKDHDIDYKDDDDKHHHHHHHHHH

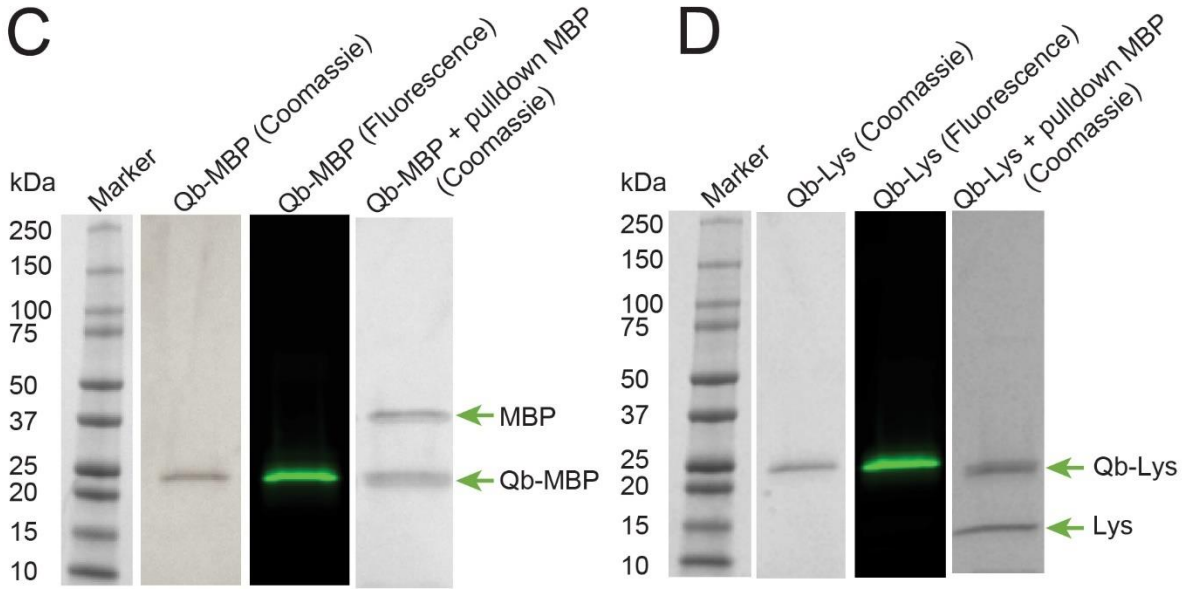

Figure S2. Quenchbody design schematic with reducing SDS-PAGE analysis of quenchbody labelling, purification and functionality (A) Protein coding sequences from either the 5M14 MBP-binding nanobody or the 1ZVH lysozyme-binding nanobody were designed with an N-terminal Cys-tag to facilitate fluorophore labelling and a C-terminal Avi-tag to facilitate biotinylation. Both a 3 x FLAG-tag and a 10 x His-tag were also included to facilitate purification procedures. The entire protein coding element was synthesised as part of an IVTT-expression DNA block containing flanking elements for cell-free expression of the quenchbodies.(B) Full peptide sequence of Qb-MBP and Qb-Lys (C) Purified Qb-MBP and (D) purified Qb-Lys were analysed by reducing SDS-PAGE and subjected to in-gel fluorescence imaging to detect TAMRA or stained with Instant Blue to assess protein purity. Quenchbody functionality was further probed by reducing SDS-PAGE analysis of pulldown assays, in which each of the Qbs were immobilised on FLAG beads and incubated with 1 µM cognate antigen prior to extensive washing and FLAG elution.

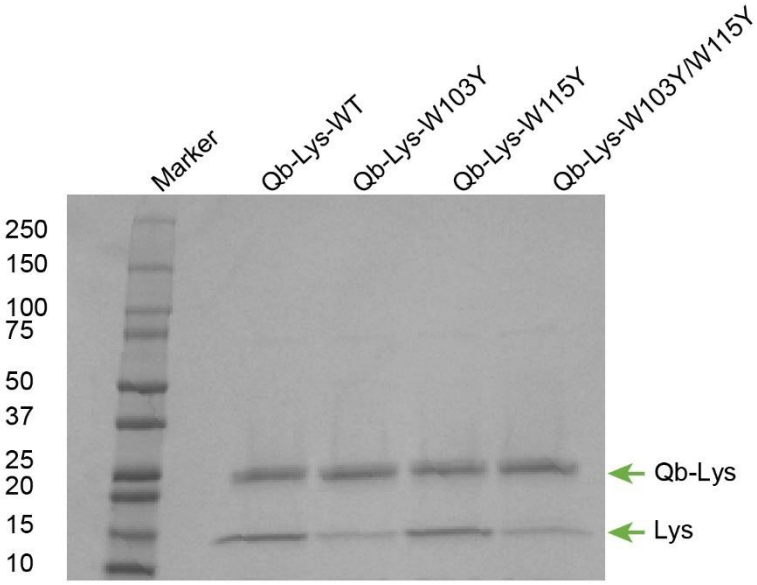

Figure S3. Lysozyme pulldown by Qb-Lys and tryptophan substitution mutants. The relative binding capacity of W103Y, W115Y and W103Y/W115Y for lysozyme was compared to the WT using a pulldown assay and analysed by reducing SDS-PAGE, showing that the W103Y substitution impacts the binding for lysozyme, but not W115Y. Note Qb-Lys-WT lane appears in Figure S1D to demonstrate pulldown.

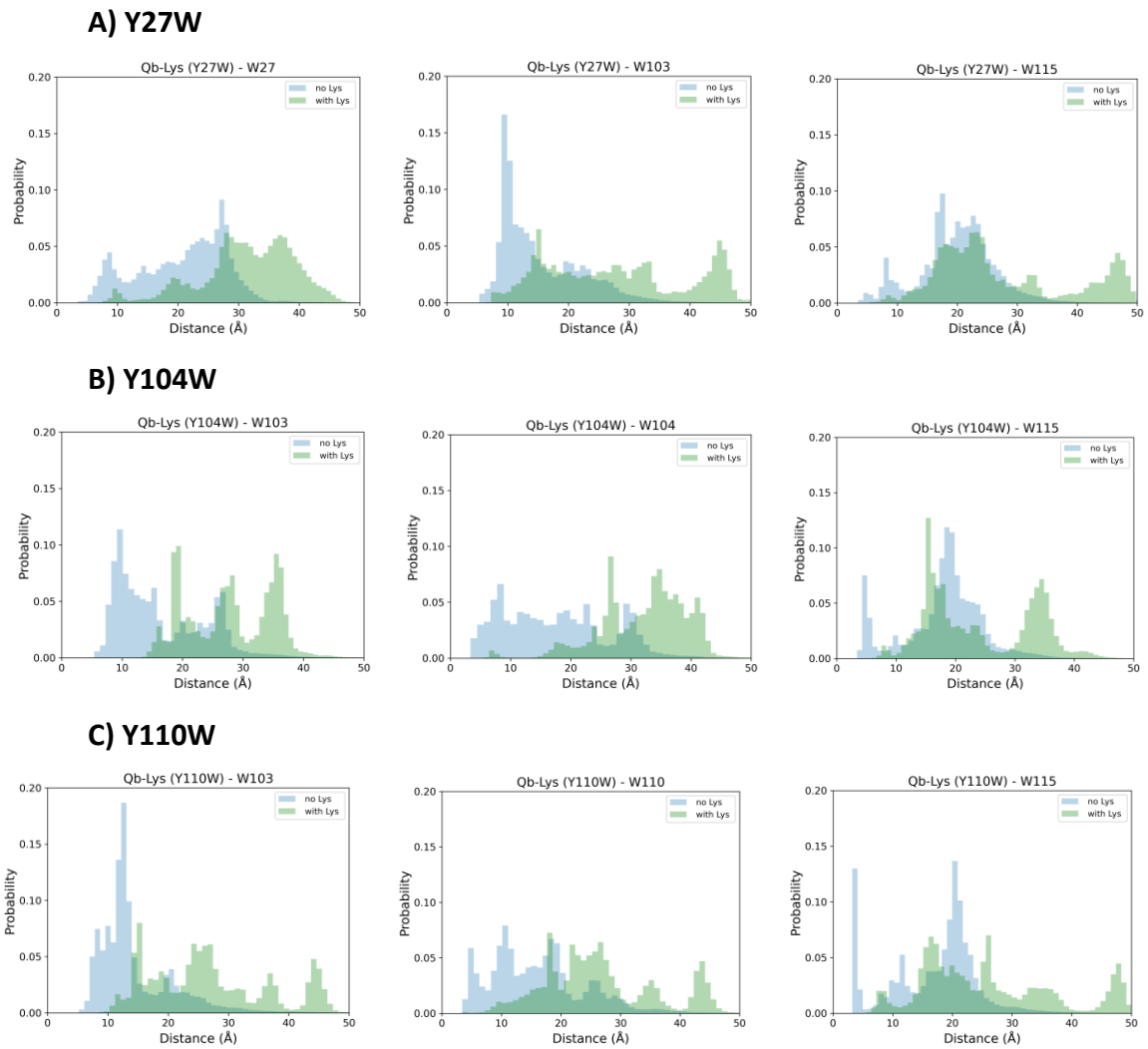

Figure S4. In silico modelling of Qb-Lys Y27W, Y104W and Y110W mutants. Normalized distribution histograms illustrating the TAMRA-CDR-tryptophan distances (W103 and W115) derived from MD simulations in the absence (blue) or presence (green) of antigen for the lysozyme-binding nanobody (PDB ID: 1ZVH). TAMRA is considered quenched by tryptophan at distances ≤ 10 Å.

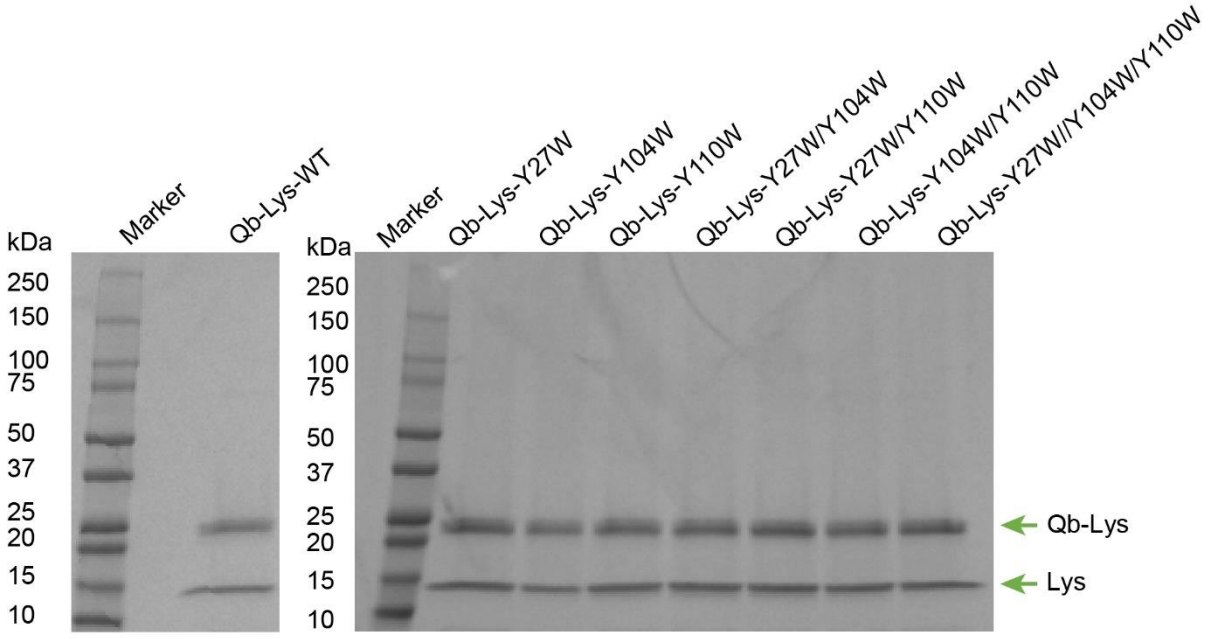

Figure S5. Lysozyme pulldown by Qb-Lys and tryptophan substitution mutants. The relative binding capacity of Y27W, Y104W, Y110W, Y27W/Y104W Y27W/Y110W,Y104W/Y110W and Y27W/Y104W/Y110W for lysozyme was assessed using a pulldown assay and analysed by reducing SDS-PAGE. Comparison to WT control from Fig S2.

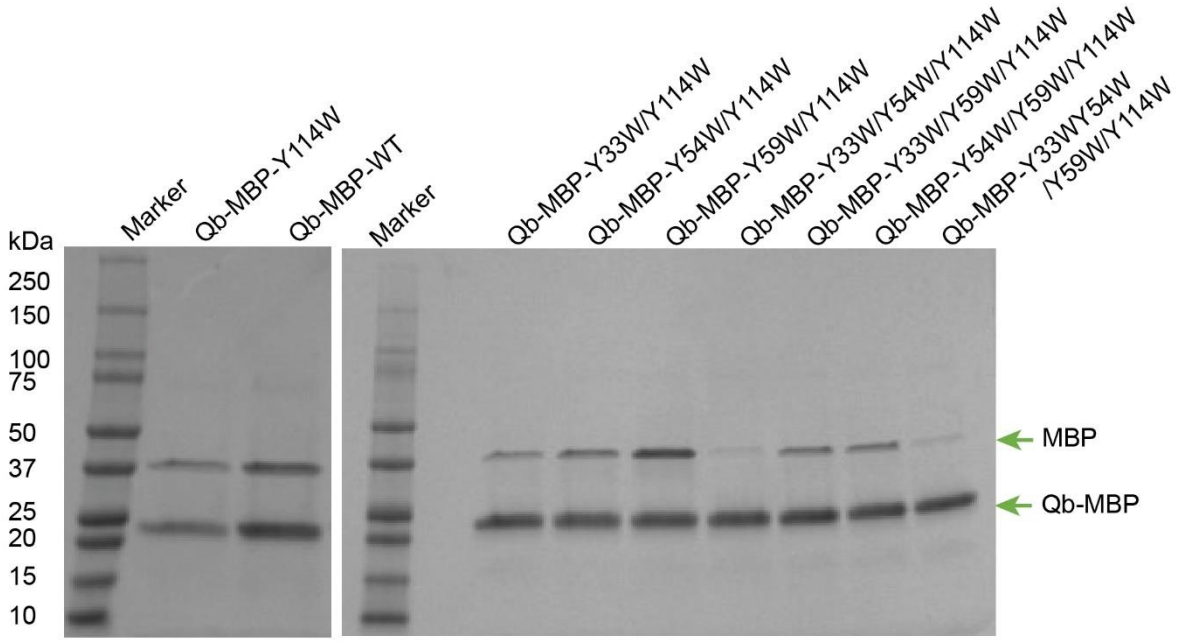

Figure S6. MBP pulldown by Qb-MBP and tryptophan substitution mutants. The relative binding capacity of Qb-MBP and variants Y114W, Y33W/Y114W, Y54W/Y114W, Y59W/Y114W, Y33W/Y54W/Y114W, Y33W/Y59W/Y114W, Y54W/Y59W/Y114W, Y33W/Y54W/Y59W/Y114W was assessed using a pulldown assay and analysed by reducing SDS-PAGE.

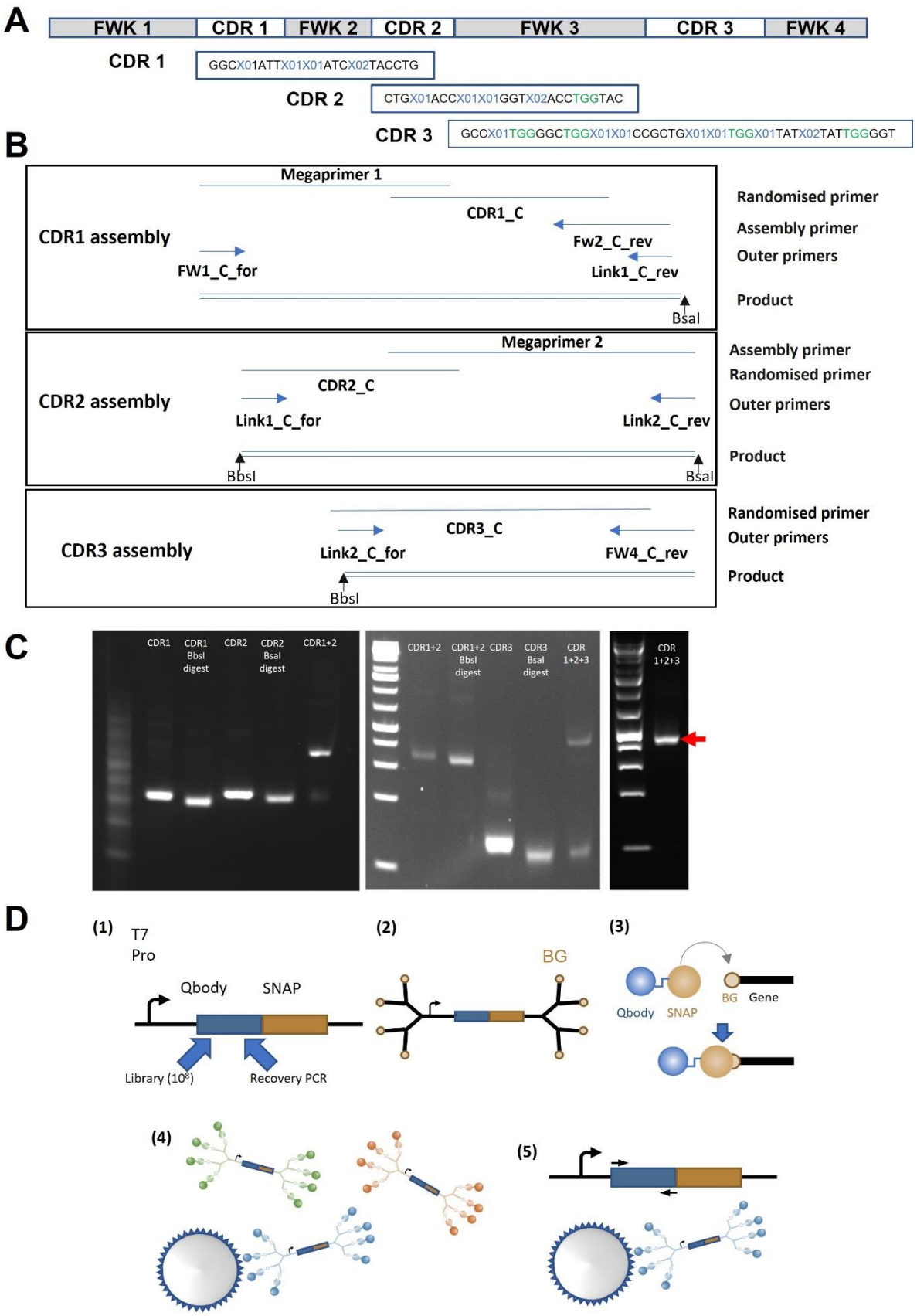
A
FWK 1
CDR 1
FWK 2
CDR 2
FWK 3
CDR 3
FWK 4
CDR 1
GGCX01ATTX01X01ATCX02TACCTG
CDR 2
CTGX01ACCX01X01GGTX02ACCTGGTAC
CDR 3
GCCX01TGGGGCTGGX01X01CCGCTGX01X01TGGX01TATX02TATTGGGGT
B
Megaprimer 1
CDR1 assembly
CDR1_C
Fw2_C_rev
FW1_C_for
Link1_C_rev
BsaI
Randomised primer
Assembly primer
Outer primers
Product
Megaprimer 2
CDR2 assembly
CDR2_C
Link1_C_for
Link2_C_rev
BbsI
BsaI
Assembly primer
Randomised primer
Outer primers
Product
CDR3 assembly
CDR3_C
Link2_C_for
FW4_C_rev
BbsI
Randomised primer
Outer primers
Product
C
CDR1
CDR1 BbsI digest
CDR2
CDR2 BsaI digest
CDR1+2
CDR1+2
CDR1+2 BbsI digest
CDR3
CDR3 BsaI digest
CDR 1+2+3
CDR 1+2+3
D
(1)
T7 Pro
Qbody
SNAP
Library (10⁸)
Recovery PCR
(2)
BG
(3)
Qbody
SNAP
BG
Gene
(4)
(5)

Figure S7. Quenchbody library assembly and SNAP display (A) Schematic of quenchbody library assembly. Tryptophan codons are indicated in green text (TGG), while randomised TRIM codons are indicated as X01 or X02 (further details available in Table S7). Location of framework (FWK) and complementarity-determining regions (CDRs), are indicated. (B) Schematic of PCR assembly fragments for CDRs 1, 2 and 3. (C) Quenchbody library assembly: (left) PCR assemblies, restriction digestion products and ligation product for CDRs 1 and 2. Center: CDR 1+2 PCR product, CDR3 PCR assembly, restriction digestion products and ligation of complete quenchbody sequence (CDRs 1, 2 and 3). Right: Completed library. (D) SNAP-display selection of human IL6 quenchbody binders. (1.) A quenchbody library is assembled at the N-terminus of the SNAP gene, separated by a G/S-rich linker. 2. Dendrimer-like DNA conjugated to benzylguanine is ligated to the expression cassette. 3. DNA libraries are encapsulated in water-in-oil emulsions with PURExpress cell-free protein expression reagent, allowing linkage of protein phenotype to genotype via SNAP linkage. 4. After protein expression, libraries are broken and selected against magnetic beads displaying IL6. After the first round, DNA was recovered by PCR and selected for a further 4 rounds (two replicates) and on uncoated (blank) beads.

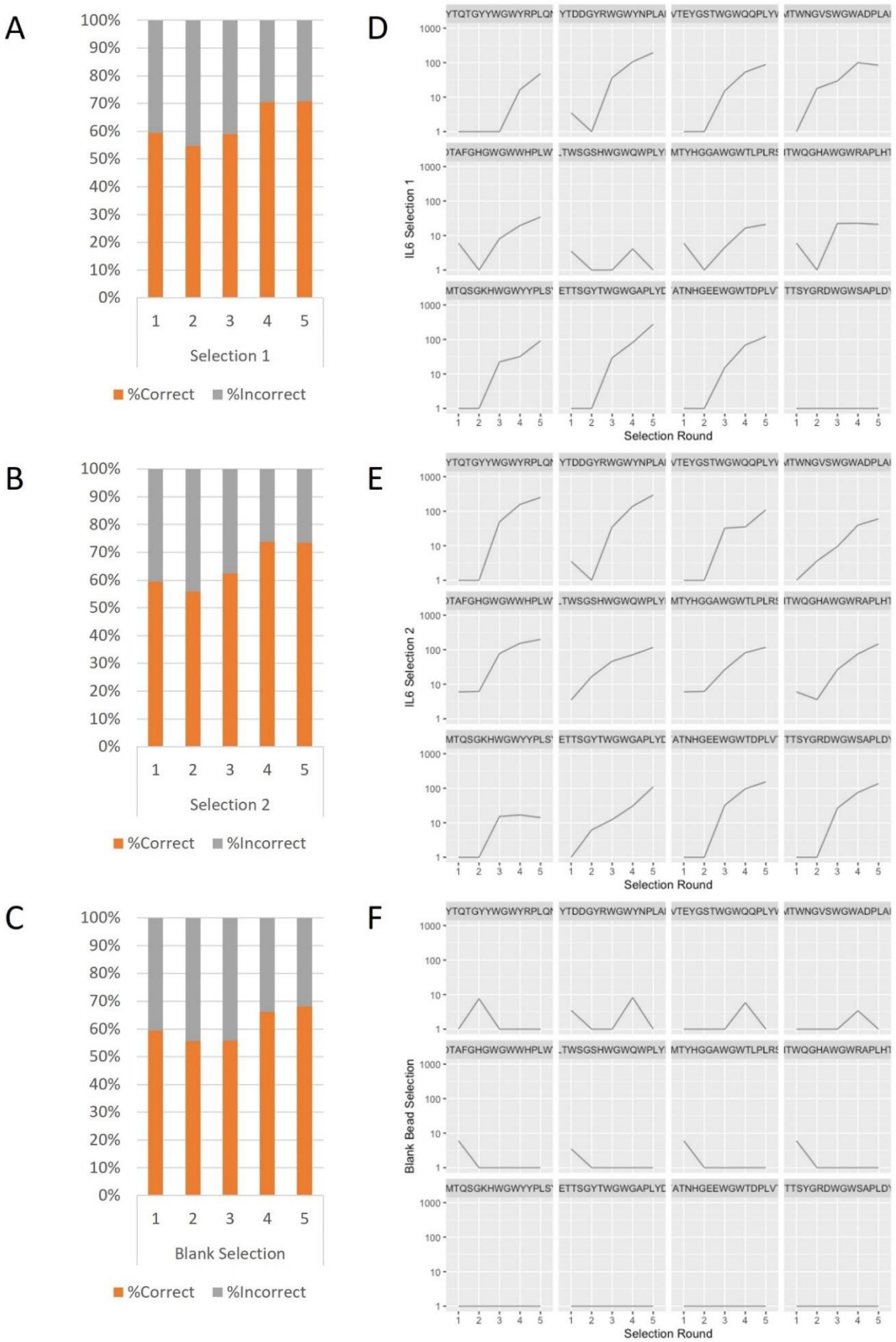

Figure S8 Assessment of IL-6 quenchbody library selections. A-C. Fraction of sequencing reads which pass filtering steps and encode a valid quenchbody protein sequence. D-F. Normalized read counts for individual quenchbody hits shown in Figure 5A, for IL-6 selections A and B, and blank bead selection.

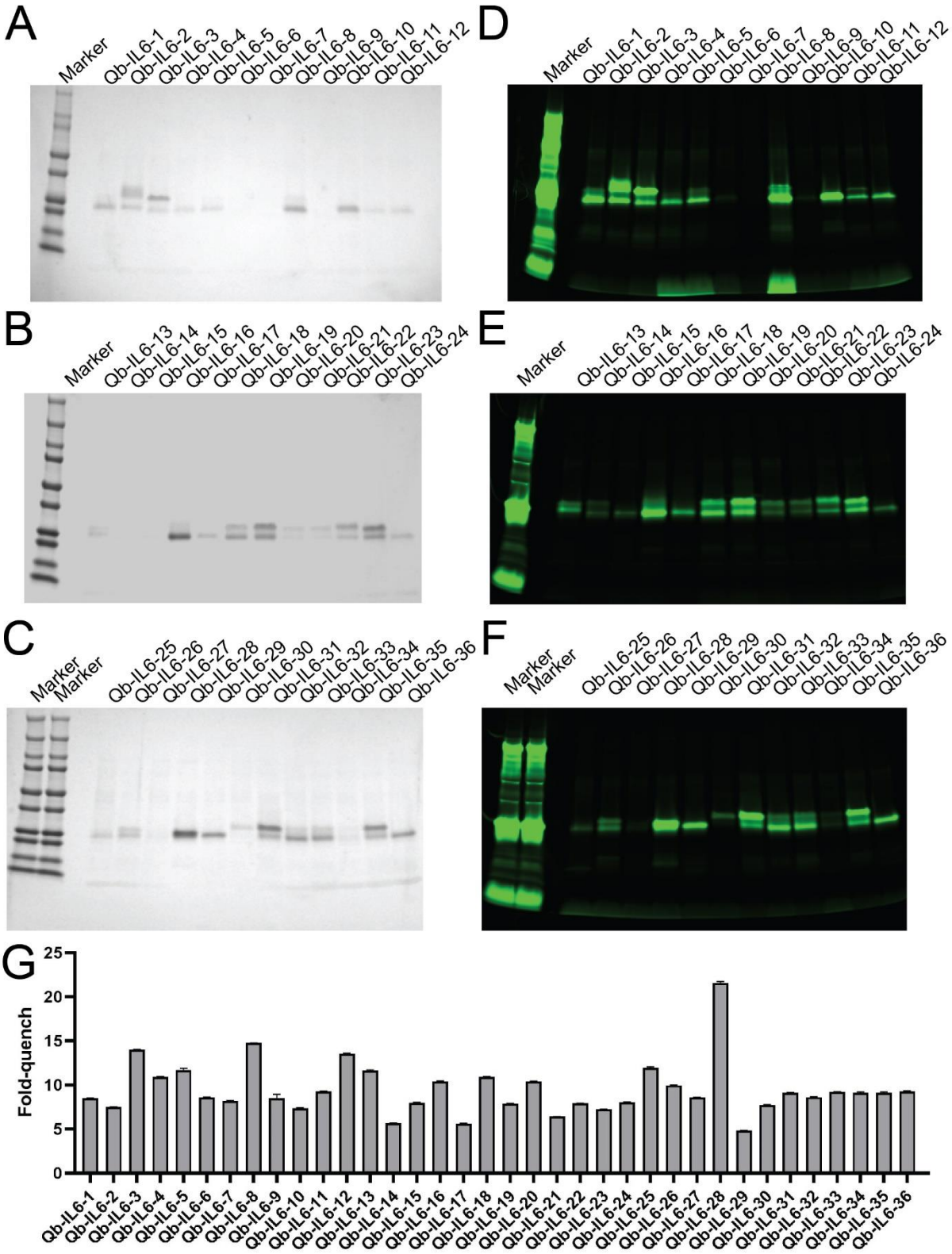

Figure S9. Reducing SDS-PAGE and fluorescent plate reader analyses showing purity, TAMRA labelling and fold-quench of quenchbodies. (A, B, C) Reducing SDS-PAGE of purified quenchbodies with Instant Blue staining to assess purity of evolved Qb-IL6-1–36. Equivalent loading of eluted constructs (10 µL), showing differences in yield obtained and structural heterogeneity as doublet bands in some instances. (D, E, F) In-gel TAMRA fluorescence of quenchbodies following reducing SDS-PAGE was assessed before Instant Blue staining on an

Amersham Typhoon Biomolecular Imager using the preset acquisition settings for Cy3 imaging (excitation = 532 nm, emission filter = 570 ± 20 nm), showing successful labelling of quenchbodies with varying degrees of free TAMRA contamination that appears to be quenchbody dependent, despite extensive washing. (G) Qb-IL6-1–36 were incubated (60 min, 25°C) in the presence of denaturant (2% SDS/5% β-mercaptoethanol) and analysed in a CLARIOstar fluorescence plate assay. Data are mean ± SD of the TAMRA fluorescence fold-increase relative to the 0 nM antigen native sample (excitation = 535 ± 20 nm and emission = 585 ± 30 nm).

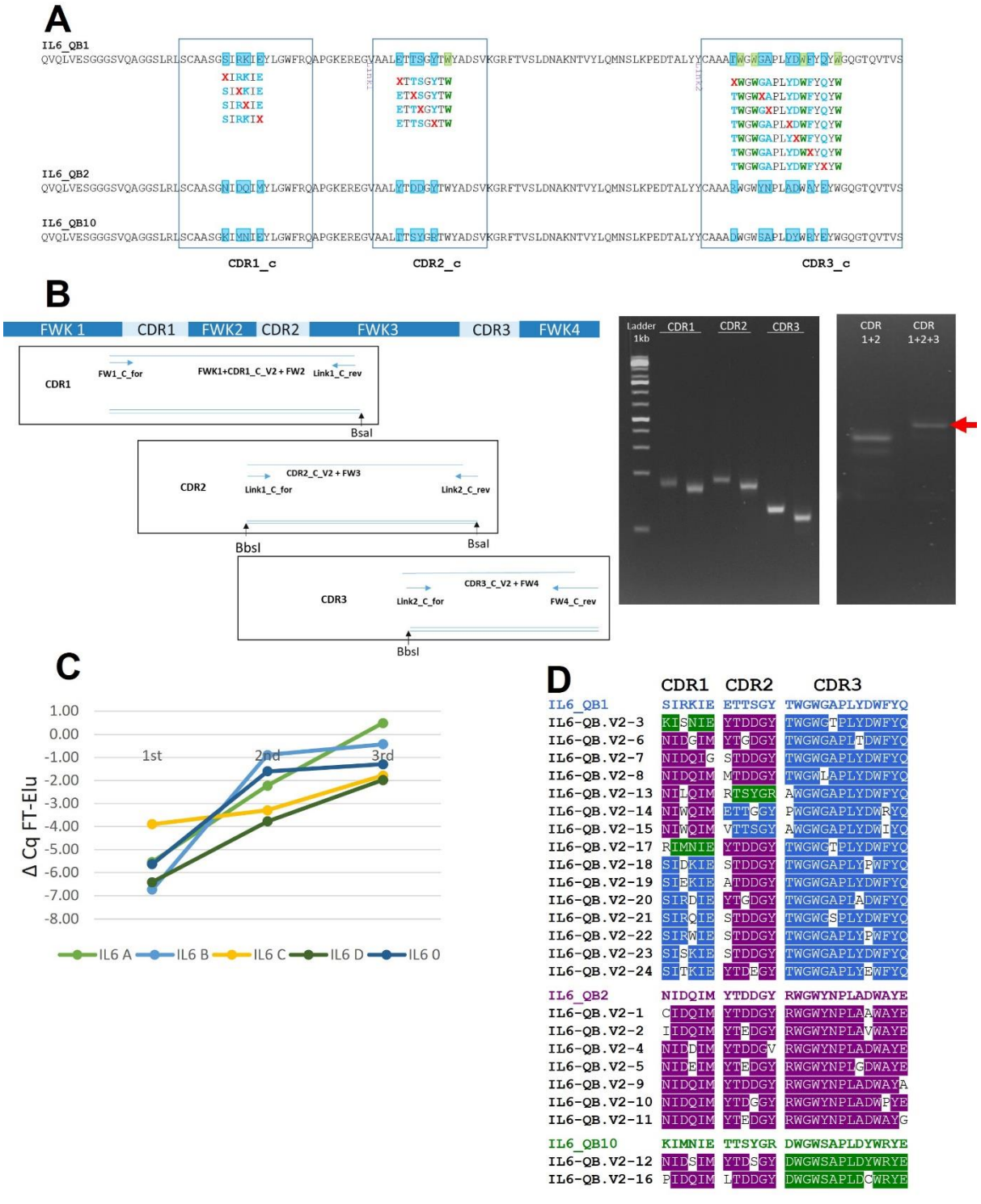

Figure S10. Library design of IL6 quenchbody for affinity maturation of Qb-IL6-1, 2 and 10. (A) Tryptophan residues are indicated in green. Mutation positions are indicated in blue and NNK codons are indicated in red. (B) Library assembly using golden gate enzymes (BsaI and BbsI), FWK: Framework. CDR: complimentary-determining region. (C) Enrichment of SNAP gene over rounds 1–3 measured by qPCR. Data points are delta Cq values of the flowthrough (FT) and elution (Elu). (D) Clustering of the affinity maturation hits to the three IL6 parent quenchbodies according to the three CDRs. Hits associated with IL6-QB1, IL6-QB2 and IL6-QB10 are indicated in blue, purple and green respectively.

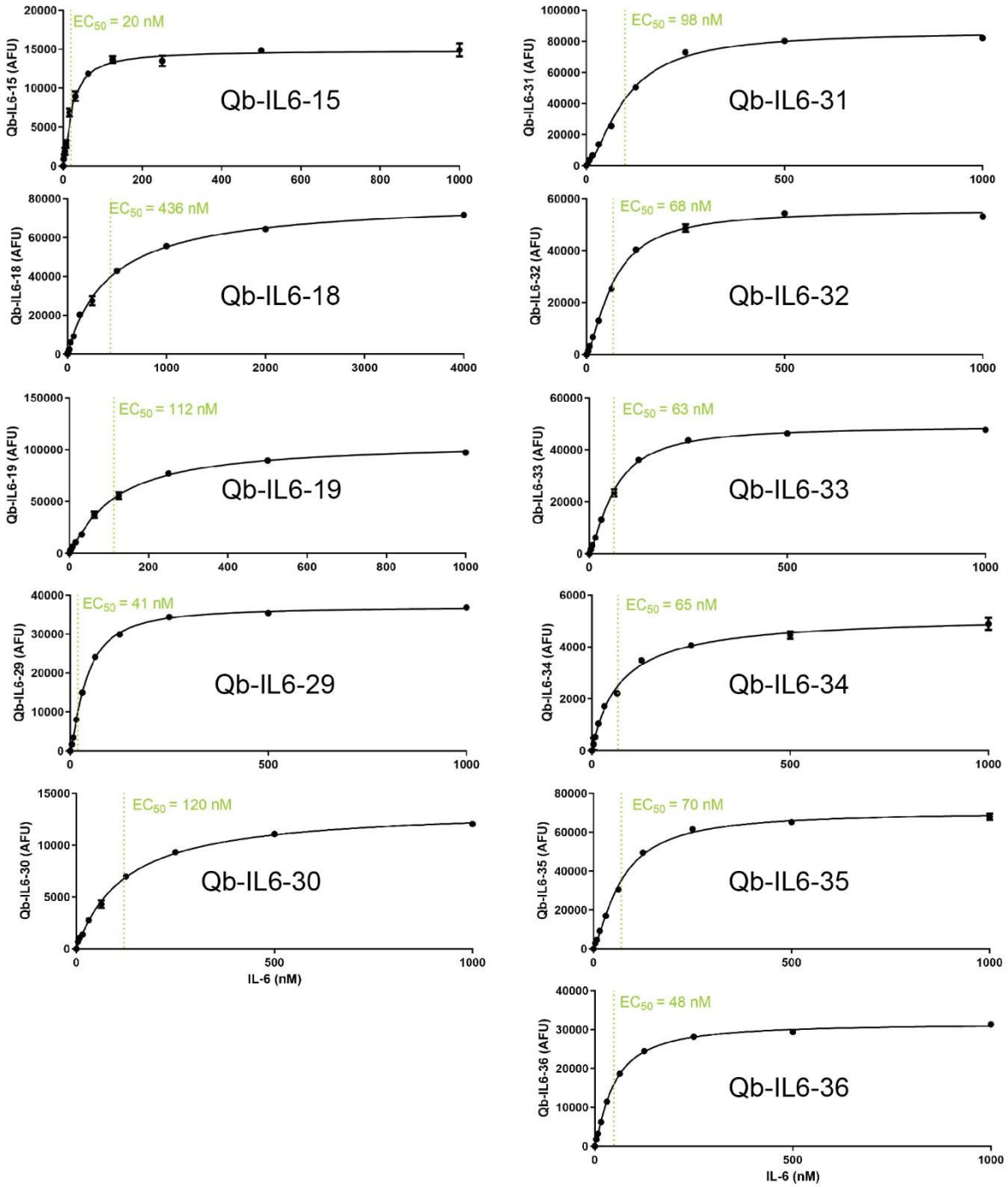

Figure S11. Fluorescence intensity changes in TAMRA-labelled IL6 quenchbodies upon antigen binding. Fluorescence intensity responses of Qb-IL6-15, 18, 19, 29, 30, 31, 32, 33, 34, 35 and 36 were analysed in a CLARIOstar fluorescence plate assay and fit to an equation describing a single site-specific binding mode to derive an EC_{50} as a proxy measure for quenchbody binding affinity (K_D). Data are mean ± SD normalised fluorescence intensity (N.F.I.) by subtracting the fluorescence (AFU) of the 0 nM antigen control from all samples.

Supplementary Materials – Tables

Table S1 Percentage time derived from MD simulations where TAMRA is within 10 Å (quenched) of the Qb-MBP exposed intrinsic tryptophans (W101, W110 and W115) in the absence and presence of MBP. Data are from six independent simulations (R1–R6) over 72 µs (R1 – R6) considering the minimum distance between any of the tryptophans and TAMRA.

	No MBP	**With MBP**
R1	75.2	0
R2	77.6	0
R3	72.4	0.4
R4	64.2	0
R5	95.6	0
R6	38.9	0
Av ± std	**70.7 ± 18.7**	**0.1 ± 0.2**

Table S2 Percentage time in Qb-Lys where TAMRA is being quenched by any of the exposed intrinsic tryptophans in the absence and presence of antigen from MD simulations. Data from the six independent simulations over 72 µs (R1 – R6) considering the minimum distance between any of the tryptophans and TAMRA.

	No Lys	**With Lys**
R1	26.1	5.3
R2	19.5	8.5
R3	14.1	0
R4	30.6	16.2
R5	58.2	5.4
R6	75.2	0
Av ± std	**37.3 ± 24.1**	**5.9 ± 6.1**

Table S3 FoldX predictions of free energy changes ($\Delta\Delta G$ in kcal/mol) of protein stability and antigen binding due to W103Y and W115Y mutations in the Qb-Lys.

Mutation	**Effect on protein stability**	**Effect on antigen binding**
W103Y	3.5 (highly destabilising)	1.0 (affects binding)
W115Y	0.6 (slightly destabilising)	0.0 (neutral)

Considering the reported accuracy of FoldX is 0.46 kcal/mol [47], mutations were considered:
highly stabilising ($\Delta\Delta G < -1.84$ kcal/mol);
stabilising (-1.84 kcal/mol $\leq \Delta\Delta G < -0.92$ kcal/mol);
slightly stabilising (-0.92 kcal/mol $\leq \Delta\Delta G < 0.46$ kcal/mol);
neutral (-0.46 kcal/mol $< \Delta\Delta G \leq 0.46$ kcal/mol);
slightly destabilising (0.46 kcal/mol $< \Delta\Delta G \leq 0.92$ kcal/mol);
destabilising (0.92 kcal/mol $< \Delta\Delta G \leq 1.84$ kcal/mol);
highly destabilising ($\Delta\Delta G > 1.84$ kcal/mol).

Table S4 Solvent accessible surface area (ASA) of Qb-MBP and Qb-Lys in the absence and presence of their respective antigens. Average ± standard deviation calculated from 1 µs MD simulations of the apo and antigen-bound states. Maximum ASA of tryptophan = 259.0 Å [72].

Residue	**Apo state (Å^2)**	**Antigen-bound state (Å^2)**
5M14 scaffold (Qb-MBP)		
W36	1.8 ± 1.6	3.3 ± 2.6
W101	165.3 ± 27.9	57.8 ± 9.0
W110	200.8 ± 22.4	66.9 ± 28.3
W115	79.4 ± 22.2	37.4 ± 11.2
1ZVH scaffold (Qb-Lys)		
W36	3.2 ± 2.3	2.6 ± 2.1
W103	60.2 ± 11.7	6.1 ± 3.5
W115	75.4 ± 9.8	77.2 ± 14.9

Table S5 Percentage time derived from MD simulations where TAMRA is within 10 Å (quenched) of the Qb-Lys introduced tryptophans in the absence and presence of lysozyme. Data is from six independent simulations (R1 – R6) over 72 µs considering the minimum distance between any of the tryptophans and TAMRA.

(A) **Y27W**

	No Lys	With Lys
R1	35.9	10.1
R2	42.4	13.0
R3	53.0	0
R4	36.8	9.5
R5	42.0	0
R6	61.8	0.4
Av ± std	**45.3 ± 10.1**	**5.5 ± 6.0**

(A) **Y104W**

	No Lys	With Lys
R1	31.7	2.6
R2	58.1	0.3
R3	76.2	0
R4	20.1	16.2
R5	84.0	0
R6	38.5	0
Av ± std	**51.4 ± 25.5**	**3.2 ± 6.5**

(B) **Y110W**

	No Lys	With Lys
R1	56.1	0
R2	80.7	25.5
R3	21.0	0.4
R4	46.8	3.1
R5	34.1	4.5
R6	38.4	7.0
Av ± std	**46.2 ± 20.6**	**6.8 ± 9.5**

Table S6 FoldX predictions of free energy changes ($\Delta\Delta G$ in kcal/mol) of protein stability and antigen binding due to Y27W, Y104W and Y110W mutations in the Qb-Lys and Qb-MBP.

Mutation	Effect on protein stability	Effect on antigen binding
Qb-Lys (PDB ID: 1ZVH)		
Y27W	0.5 (slightly destabilising)	-0.3 (neutral)
Y104W	0.2 (neutral)	0.4 (neutral)
Y110W	-0.1 (neutral)	1.3 (affects binding)
Qb-MBP (PDB ID: 5M14)		
G32W	-0.0 (neutral)	6.3 (highly affects binding)
Y33W	1.8 (highly destabilising)	2.1 (highly affects binding)
Y54W	1.5 (destabilising)	0.6 (slightly affects binding)
Y59W	-0.2 (neutral)	1.0 (affects binding)
Y114W	-0.2 (neutral)	0.2 (neutral)
W101A	3.1 (highly destabilising)	3.2 (highly affects binding)
W110A	1.2 (destabilising)	1.3 (affects binding)
W115A	4.3 (highly destabilising)	1.1 (affects binding)

Considering the reported accuracy of FoldX is 0.46 kcal/mol [47], mutations were considered:
highly stabilising ($\Delta\Delta G < -1.84$ kcal/mol);
stabilising (-1.84 kcal/mol $\leq \Delta\Delta G < -0.92$ kcal/mol);
slightly stabilising (-0.92 kcal/mol $\leq \Delta\Delta G < 0.46$ kcal/mol);
neutral (-0.46 kcal/mol $< \Delta\Delta G \leq 0.46$ kcal/mol);
slightly destabilising (0.46 kcal/mol $< \Delta\Delta G \leq 0.92$ kcal/mol);
destabilising (0.92 kcal/mol $< \Delta\Delta G \leq 1.84$ kcal/mol);
highly destabilising ($\Delta\Delta G > 1.84$ kcal/mol).

Table S7 Frequency % of each amino acid (AA) in the randomised TRIM positions X01 and X02

AA		Codon	X01	X02
K	Lys	AAA	5.00	7.50
N	Asn	AAC	10.60	7.50
T	Thr	ACC	10.60	10.00
I	Ile	ATC	2.00	2.00
M	Met	ATG	2.00	2.00
Q	Gln	CAG	5.00	7.50
H	His	CAT	5.00	7.50
P	Pro	CCA		
R	Arg	CGT	5.00	7.50
L	Leu	CTG	2.00	2.00
E	Glu	GAA	5.00	7.50
D	Asp	GAT	5.00	
A	Ala	GCA	10.60	
G	Gly	GGT	2.00	7.50
V	Val	GTT	2.00	2.00
Y	Tyr	TAC	10.60	10.00
S	Ser	TCT	10.60	10.00
C	Cys	TGC		
W	Trp	TGG	5.00	7.50
F	Phe	TTC	2.00	2.00

Acknowledgements

Parts of this research were supported by the Australian Research Council Centre of Excellence in Quantum Biotechnology through project number CE230100021. This project was undertaken with the assistance of resources and services from the National Computational Infrastructure (NCI), which is supported by the Australian Government. This work was supported by the Australian National Health and Medical Research Council (Investigator grant 2007778 to L.M.S.) and the Human Frontiers of Science Program (Program grant RGP0021/2020 to A.D.G. and A.M.v.O.).

Competing Interests

This work was financially supported by Quantum-Si . Marco Ribezzi-Crivellari and Sebastian Hutchinson are employed by Quantum-Si. Antoine van Oijen and Andrew Griffiths are members of the Quantum-Si Scientific Advisory Committee.

References

1. Hristova, V.A. and D.W. Chan, *Cancer biomarker discovery and translation: proteomics and beyond.* Expert Rev Proteomics, 2019. **16**(2): p. 93-103.
2. Crutchfield, C.A., et al., *Advances in mass spectrometry-based clinical biomarker discovery.* Clinical Proteomics, 2016. **13**(1).
3. Geyer, P.E., et al., *Revisiting biomarker discovery by plasma proteomics.* Molecular Systems Biology, 2017. **13**(9).
4. Hawkridge, A.M. and D.C. Muddiman, *Mass spectrometry-based biomarker discovery: Toward a global proteome index of individuality.* Annual Review of Analytical Chemistry, 2009. **2**: p. 265-277.
5. Alfaleh, M.A., et al., *Phage Display Derived Monoclonal Antibodies: From Bench to Bedside.* Front Immunol, 2020. **11**: p. 1986.
6. Bazan, J., I. Całkosiński, and A. Gamian, *Phage display--a powerful technique for immunotherapy: 1. Introduction and potential of therapeutic applications.* Hum Vaccin Immunother, 2012. **8**(12): p. 1817-28.
7. Ledsgaard, L., et al., *Basics of Antibody Phage Display Technology.* Toxins (Basel), 2018. **10**(6).
8. Pande, J., M.M. Szewczyk, and A.K. Grover, *Phage display: concept, innovations, applications and future.* Biotechnol Adv, 2010. **28**(6): p. 849-58.
9. Hage, D.S., *Immunoassays.* Analytical Chemistry, 1999. **71**(12): p. 294R-304R.
10. Vashist, S.K. and J.H.T. Luong, *Immunoassays: An overview*, in *Handbook of Immunoassay Technologies: Approaches, Performances, and Applications*. 2018, Elsevier. p. 1-18.
11. Ouchi, N., et al., *Novel modulator for endothelial adhesion molecules: Adipocyte-derived plasma protein adiponectin.* Circulation, 1999. **100**(25): p. 2473-2476.
12. Koczula, K.M. and A. Gallotta, *Lateral flow assays.* Essays Biochem, 2016. **60**(1): p. 111-20.
13. Beaudet, L., et al., *AlphaLISA immunoassays: the no-wash alternative to ELISAs for research and drug discovery.* Nature Methods, 2008. **5**(12): p. an8-an9.
14. Bielefeld-Sevigny, M., *AlphaLISA immunoassay platform- the "no-Wash" high-throughput alternative to ELISA.* Assay and Drug Development Technologies, 2009. **7**(1): p. 90-92.
15. Abe, R., et al., *"quenchbodies": Quench-based antibody probes that show antigen-dependent fluorescence.* Journal of the American Chemical Society, 2011. **133**(43): p. 17386-17394.

16. Dong, J. and H. Ueda, *Recent advances in quenchbody, a fluorescent immunosensor.* Sensors (Switzerland), 2021. **21**(4): p. 1-18.
17. Ueda, H. and J. Dong, *From fluorescence polarization to Quenchbody: Recent progress in fluorescent reagentless biosensors based on antibody and other binding proteins.* Biochimica et Biophysica Acta - Proteins and Proteomics, 2014. **1844**(11): p. 1951-1959.
18. Page, C.C., et al., *Natural engineering principles of electron tunnelling in biological oxidation-reduction.* Nature, 1999. **402**(6757): p. 47-52.
19. Doose, S., H. Neuweiler, and M. Sauer, *A close look at fluorescence quenching of organic dyes by tryptophan.* Chemphyschem : a European journal of chemical physics and physical chemistry, 2005. **6**(11): p. 2277-2285.
20. Doose, S., H. Neuweiler, and M. Sauer, *Fluorescence quenching by photoinduced electron transfer: a reporter for conformational dynamics of macromolecules.* Chemphyschem, 2009. **10**(9-10): p. 1389-98.
21. Inoue, A., et al., *Creation of a Nanobody-Based Fluorescent Immunosensor Mini Q-body for Rapid Signal-On Detection of Small Hapten Methotrexate.* ACS Sensors, 2020. **5**(11): p. 3457-3464.
22. Inoue, A., et al., *Evaluation and selection of potent fluorescent immunosensors by combining fluorescent peptide and nanobodies displayed on yeast surface.* Scientific Reports, 2021. **11**(1).
23. Harmsen, M.M. and H.J. De Haard, *Properties, production, and applications of camelid single-domain antibody fragments.* Applied Microbiology and Biotechnology, 2007. **77**(1): p. 13-22.
24. Jeong, H.J., *Quenchbodies That Enable One-Pot Detection of Antigens: A Structural Perspective.* Bioengineering (Basel), 2023. **10**(11).
25. Jeong, H.-J., et al., *Development of a Quenchbody for the Detection and Imaging of the Cancer-Related Tight-Junction-Associated Membrane Protein Claudin.* Analytical Chemistry, 2017. **89**(20): p. 10783-10789.
26. Dong, J., et al., *Detection and destruction of HER2-positive cancer cells by Ultra Quenchbody-siRNA complex.* Biotechnol Bioeng, 2020. **117**(5): p. 1259-1269.
27. Jeong, H.J., J. Dong, and H. Ueda, *Single-Step Detection of the Influenza Virus Hemagglutinin Using Bacterially-Produced Quenchbodies.* Sensors (Basel), 2018. **19**(1).
28. De Genst, E., et al., *Molecular basis for the preferential cleft recognition by dromedary heavy-chain antibodies.* Proceedings of the National Academy of Sciences of the United States of America, 2006. **103**(12): p. 4586-4591.
29. Zimmermann, I., et al., *Synthetic single domain antibodies for the conformational trapping of membrane proteins.* eLife, 2018. **7**.
30. Martí-Renom, M.A., et al., *Comparative Protein Structure Modeling of Genes and Genomes.* Annual Review of Biophysics and Biomolecular Structure, 2000. **29**(1): p. 291-325.
31. Jo, S., et al., *CHARMM-GUI: A web-based graphical user interface for CHARMM.* Journal of Computational Chemistry, 2008. **29**(11): p. 1859-1865.
32. Vanommeslaeghe, K., et al., *CHARMM general force field: A force field for drug-like molecules compatible with the CHARMM all-atom additive biological force fields.* J Comput Chem, 2010. **31**(4): p. 671-90.
33. Jorgensen, W.L., et al., *Comparison of simple potential functions for simulating liquid water.* The Journal of Chemical Physics, 1983. **79**(2): p. 926-935.
34. Phillips, J.C., et al., *Scalable molecular dynamics on CPU and GPU architectures with NAMD.* J Chem Phys, 2020. **153**(4): p. 044130.
35. Olsson, M.H.M., et al., *PROPKA3: Consistent Treatment of Internal and Surface Residues in Empirical pKa Predictions.* Journal of Chemical Theory and Computation, 2011. **7**(2): p. 525-537.

36. Brünger, A., C.L. Brooks, and M. Karplus, *Stochastic boundary conditions for molecular dynamics simulations of ST2 water.* Chemical Physics Letters, 1984. **105**(5): p. 495-500.
37. Feller, S.E., et al., *Constant pressure molecular dynamics simulation: The Langevin piston method.* The Journal of Chemical Physics, 1995. **103**(11): p. 4613-4621.
38. Hopkins, C.W., et al., *Long-Time-Step Molecular Dynamics through Hydrogen Mass Repartitioning.* Journal of Chemical Theory and Computation, 2015. **11**(4): p. 1864-1874.
39. Andersen, H.C., *Rattle: A "velocity" version of the shake algorithm for molecular dynamics calculations.* Journal of Computational Physics, 1983. **52**(1): p. 24-34.
40. Darden, T., D. York, and L. Pedersen, *Particle mesh Ewald: An N·log(N) method for Ewald sums in large systems.* The Journal of Chemical Physics, 1993. **98**(12): p. 10089-10092.
41. Humphrey, W., A. Dalke, and K. Schulten, *VMD: visual molecular dynamics.* J Mol Graph, 1996. **14**(1): p. 33-8, 27-8.
42. Romo, T.D. and A. Grossfield, *LOOS: an extensible platform for the structural analysis of simulations.* Annu Int Conf IEEE Eng Med Biol Soc, 2009. **2009**: p. 2332-5.
43. Michaud-Agrawal, N., et al., *MDAnalysis: a toolkit for the analysis of molecular dynamics simulations.* J Comput Chem, 2011. **32**(10): p. 2319-27.
44. Meng, E.C., et al., *UCSF ChimeraX: Tools for structure building and analysis.* Protein Science, 2023. **32**(11).
45. Pettersen, E.F., et al., *UCSF Chimera--a visualization system for exploratory research and analysis.* J Comput Chem, 2004. **25**(13): p. 1605-12.
46. Pettersen, E.F., et al., *UCSF ChimeraX: Structure visualization for researchers, educators, and developers.* Protein Science, 2021. **30**(1): p. 70-82.
47. Schymkowitz, J., et al., *The FoldX web server: an online force field.* Nucleic Acids Research, 2005. **33**(suppl_2): p. W382-W388.
48. Shimizu, Y., et al., *Cell-free translation reconstituted with purified components.* Nature Biotechnology, 2001. **19**(8): p. 751-755.
49. Wilkins, M.R., et al., *Protein identification and analysis tools in the ExPASy server.* Methods in molecular biology (Clifton, N.J.), 1999. **112**: p. 531-552.
50. Lewis, J.S., et al., *Single-molecule visualization of Saccharomyces cerevisiae leading-strand synthesis reveals dynamic interaction between MTC and the replisome.* Proc Natl Acad Sci U S A, 2017. **114**(40): p. 10630-10635.
51. Lewis, J.S., et al., *Tunability of DNA Polymerase Stability during Eukaryotic DNA Replication.* Mol Cell, 2020. **77**(1): p. 17-25.e5.
52. Mueller, S.H., et al., *Rapid single-molecule characterisation of enzymes involved in nucleic-acid metabolism.* Nucleic Acids Res, 2023. **51**(1): p. e5.
53. Kaltenbach, M., V. Stein, and F. Hollfelder, *SNAP dendrimers: multivalent protein display on dendrimer-like DNA for directed evolution.* Chembiochem, 2011. **12**(14): p. 2208-16.
54. Truong, T.T.T., et al., *Studying the characteristics of nanobody CDR regions based on sequence analysis in combination with 3D structures.* J Genet Eng Biotechnol, 2022. **20**(1): p. 157.
55. Marmé, N., et al., *Inter- and Intramolecular Fluorescence Quenching of Organic Dyes by Tryptophan.* Bioconjugate Chemistry, 2003. **14**(6): p. 1133-1139.
56. Vaiana, A.C., et al., *Fluorescence Quenching of Dyes by Tryptophan: Interactions at Atomic Detail from Combination of Experiment and Computer Simulation.* Journal of the American Chemical Society, 2003. **125**(47): p. 14564-14572.
57. Marmé, N., et al., *Inter- and Intramolecular Fluorescence Quenching of Organic Dyes by Tryptophan.* Bioconjugate Chemistry, 2003. **14**(6): p. 1133-1139.
58. Chen, H., et al., *Mechanisms of quenching of Alexa fluorophores by natural amino acids.* J Am Chem Soc, 2010. **132**(21): p. 7244-5.
59. Kaltenbach, M. and F. Hollfelder, *SNAP display: in vitro protein evolution in microdroplets.* Methods in molecular biology, 2012. **805**: p. 101-11.

60. Tanaka, T., M. Narazaki, and T. Kishimoto, *IL-6 in inflammation, immunity, and disease.* Cold Spring Harb Perspect Biol, 2014. **6**(10): p. a016295.
61. Mori, Y., et al., *Antigen-dependent fluorescence response of anti-c-Myc Quenchbody studied by molecular dynamics simulations.* Chemical Physics Letters, 2018. **698**: p. 223-226.
62. Jeong, H.J., et al., *Construction of dye-stapled Quenchbodies by photochemical crosslinking to antibody nucleotide-binding sites.* Chem Commun (Camb), 2017. **53**(73): p. 10200-10203.
63. Dong, J., et al., *Construction of Quenchbodies to detect and image amyloid β oligomers.* Analytical Biochemistry, 2018. **550**: p. 61-67.
64. Dong, J., et al., *PM Q-probe: A fluorescent binding protein that converts many antibodies to a fluorescent biosensor.* Biosensors and Bioelectronics, 2020. **165**: p. 112425.
65. Dong, J., et al., *VH-Based Mini Q-Body: A Novel Quench-Based Immunosensor.* Sensors, 2023. **23**(4).
66. Dong, J., et al., *Detection and destruction of HER2-positive cancer cells by Ultra Quenchbody-siRNA complex.* Biotechnology and Bioengineering, 2020. **117**(5): p. 1259-1269.
67. Jeong, H.J., et al., *Detection of vimentin serine phosphorylation by multicolor Quenchbodies.* Biosens Bioelectron, 2013. **40**(1): p. 17-23.
68. Abe, R., et al., *Ultra Q-bodies: quench-based antibody probes that utilize dye-dye interactions with enhanced antigen-dependent fluorescence.* Scientific Reports, 2014. **4**(1): p. 4640.
69. Said, E.A., et al., *Defining IL-6 levels in healthy individuals: A meta-analysis.* J Med Virol, 2021. **93**(6): p. 3915-3924.
70. Martin, H., B. Olander, and M. Norman, *Reactive hyperemia and interleukin 6, interleukin 8, and tumor necrosis factor-alpha in the diagnosis of early-onset neonatal sepsis.* Pediatrics, 2001. **108**(4): p. E61.
71. Fridy, P.C., et al., *A robust pipeline for rapid production of versatile nanobody repertoires.* Nat Methods, 2014. **11**(12): p. 1253-60.
72. Miller, S., et al., *Interior and surface of monomeric proteins.* Journal of Molecular Biology, 1987. **196**(3): p. 641-656.